Nanoscale Horizons

The home for rapid reports of exceptional significance in nanoscience and nanotechnology

rsc.li/nanoscale-horizons

ROYAL SOCIETY
OF **CHEMISTRY**
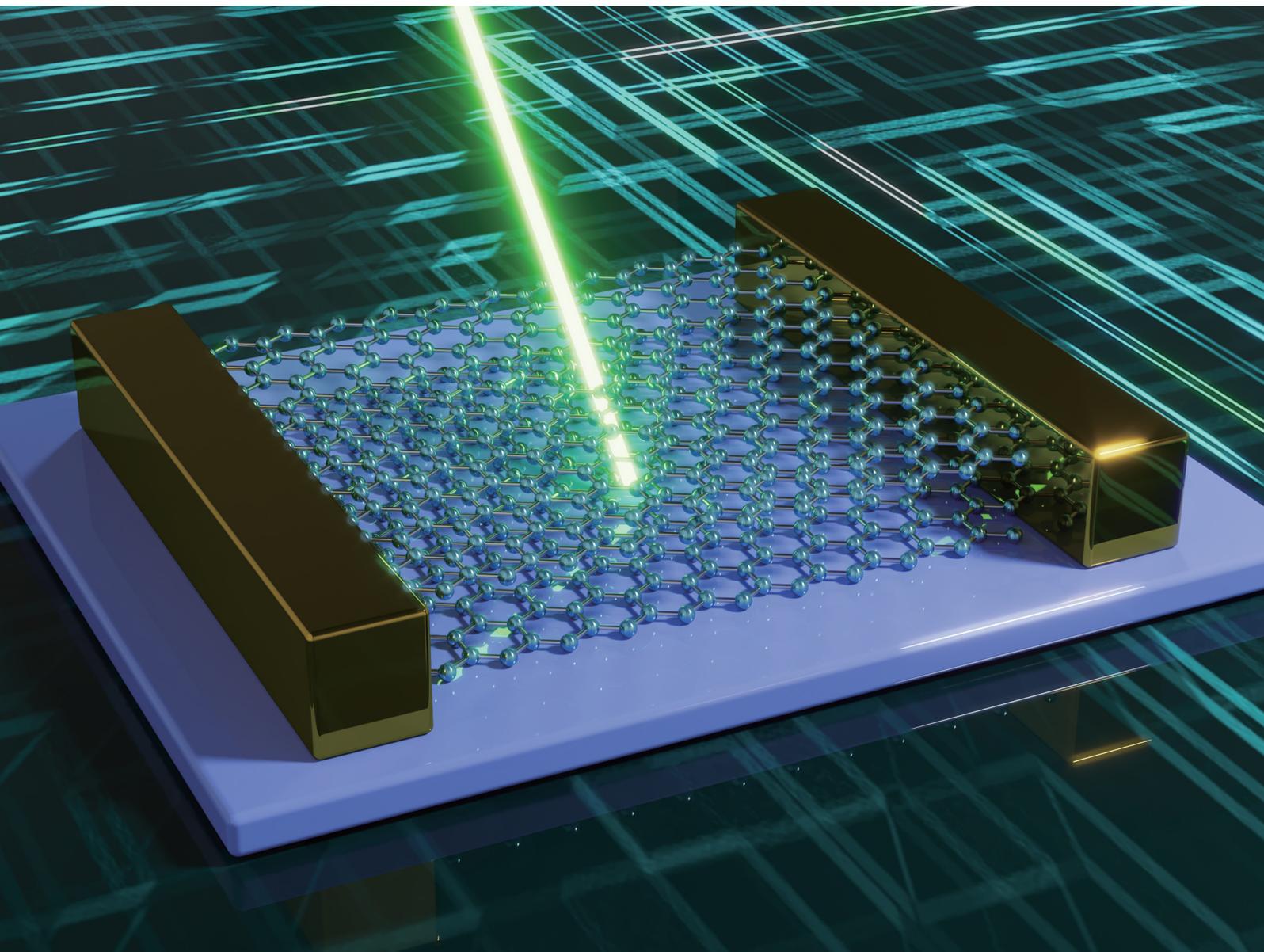
REVIEW ARTICLE
Xinyue Liu, Zhaoqiang Zheng, Jiandong Yao *et al.*
Two-dimensional layered material photodetectors: what could be the upcoming downstream applications beyond prototype devices?

NCNST

Nanoscale Horizons

REVIEW

Check for updates

Two-dimensional layered material photodetectors: what could be the upcoming downstream applications beyond prototype devices?

Yuhang Ma,†[ab] Huanrong Liang,†[ab] Xinyi Guan, [ID][a] Shuhua Xu,[a] Meiling Tao,[a] Xinyue Liu, [ID]*[c] Zhaoqiang Zheng, [ID]*[d] Jiandong Yao [ID]*[ab] and Guowei Yang [ID][ab]

With distinctive advantages spanning excellent flexibility, rich physical properties, strong electrostatic tunability, dangling-bond-free surface, and ease of integration, 2D layered materials (2DLMs) have demonstrated tremendous potential for photodetection. However, to date, most of the research enthusiasm has been merely focused on developing novel prototype devices. In the past few years, researchers have also been devoted to developing various downstream applications based on 2DLM photodetectors to contribute to promoting them from fundamental research to practical commercialization, and extensive accomplishments have been realized. In spite of the remarkable advancements, these fascinating research findings are relatively scattered. To date, there is still a lack of a systematic and profound summarization regarding this fast-evolving domain. This is not beneficial to researchers, especially researchers just entering this research field, who want to have a quick, timely, and comprehensive inspection of this fascinating domain. To address this issue, in this review, the emerging downstream applications of 2DLM photodetectors in extensive fields, including imaging, health monitoring, target tracking, optoelectronic logic operation, ultraviolet monitoring, optical communications, automatic driving, and acoustic signal detection, have been systematically summarized, with the focus on the underlying working mechanisms. At the end, the ongoing challenges of this rapidly progressing domain are identified, and the potential schemes to address them are envisioned, which aim at navigating the future exploration as well as fully exerting the pivotal roles of 2DLMs towards the practical optoelectronic industry.

1. Introduction

Photodetectors represent functional electronic devices that can convert light signals into electrical signals.[1–5] These devices can respond to light irradiation by absorbing incident photons and stimulating electron–hole pairs, thereby generating additional electrical signals that are easily processed in circuits. To date,

[a] *State Key Laboratory of Optoelectronic Materials and Technologies, Nanotechnology Research Center, School of Materials Science & Engineering, Sun Yat-sen University, Guangzhou 510275, Guangdong, P. R. China. E-mail: yaojd3@mail.sysu.edu.cn*

[b] *Guangzhou Key Laboratory of Flexible Electronic Materials and Wearable Devices, Sun Yat-sen University, Guangzhou 510275, Guangdong, P. R. China*

[c] *Guangdong Provincial Key Laboratory of Nanophotonic Manipulation, Institute of Nanophotonics, Jinan University, Guangzhou 511443, China. E-mail: liuxinyue8@jnu.edu.cn*

[d] *School of Materials and Energy, Guangdong University of Technology, Guangzhou 510006, Guangdong, P. R. China. E-mail: zhengzhq5@mail2.sysu.edu.cn*

† These authors contributed equally to this work.

photodetectors have been exploited in extensive domains, including communications,[6,7] imaging,[8,9] clinical diagnostics,[10] artificial photonic nociceptors,[11] *etc.* With the continual progress of science and technology, the application scope of photodetectors is also constantly expanding, bringing more convenience, opportunities, and possibilities to people's lives and work.

Traditional optoelectronic devices have mainly relied on bulk covalent semiconductors such as silicon, germanium, gallium arsenide, lead sulfide, mercury cadmium telluride, *etc.* The constituent atoms of these materials are interconnected through strong covalent bonds along any direction, which makes the preparation and processing of the corresponding photodetectors quite complex and costly. In addition, these bulk materials suffer from high brittleness, making it difficult for them to be competent for wearable forms that need to undergo bending, folding, and stretching. Furthermore, traditional covalent photosensitive materials are easily degraded by environmental factors such as temperature and

humidity on account of their interceptive surfaces terminated with a large number of active dangling bonds, resulting in unstable photosensitive performance and easy aging/degradation, especially under low-dimensional conditions (*i.e.* high surface-to-volume ratio). Meanwhile, the numerous interfacial defect states can lead to high background noise and low photosensitivity for the optoelectronic devices based on these materials, thus requiring complex peripheral circuits/noise reduction systems (such as cooling devices) to improve the detection performance of related devices. In consideration of the above formidable challenges, it is essential to search for alternative materials.

Two-dimensional layered materials (2DLMs) are a new family of low-dimensional phase represented by graphene (Gr) and MoS_2. This category of materials is composed of a single monolayer or a few self-passivated monolayers. The interactions between the monolayers are weak van der Waals (vdW) forces, while the interactions between atoms within the same monolayer are usually strong covalent bonds.[12–16]

Compared to traditional bulk covalent semiconductors, 2DLMs manifest a handful of unique advantages. Firstly, due to the extremely thin thickness, 2DLMs exhibit excellent flexibility and conformability. These characteristics allow them to be flexibly integrated on various surfaces, greatly expanding their potential application scenarios and making them widely applicable in wearable devices. Meanwhile, the low-dimensional properties of 2DLMs warrant excellent electrostatic tunability, providing a substantial degree of freedom for device performance modulation. Secondly, the surface of 2DLMs is free of dangling bonds, which markedly reduces the interfacial defects, contributing to suppressing device noise and improving the transport characteristics of charge carriers, thereby improving the photosensitivity of the devices. Meanwhile, such unique structural characteristics allow the construction of 2DLM based heterojunctions to be unconstrained by the lattice-matching conditions.[17–32] Therefore, theoretically, the manipulation of photocarrier dynamics and multifunctional photodetection can be achieved through the stacking and

Yuhang Ma obtained his BS degree from Sun Yat-sen University in 2022. He is now studying for his MA degree under the supervision of Prof. Jiandong Yao at the State Key Laboratory of Optoelectronic Materials and Technologies, School of Materials Science & Engineering, Sun Yat-sen University. His current research focuses on pulsed-laser deposition synthesis of low-dimensional materials, design and fabrication of novel photodetectors, and their applications based on optoelectronic properties.

Yuhang Ma

Huanrong Liang graduated from Sun Yat-sen University and received his BS degree in materials chemistry in 2023. He continues his graduate study under the supervision of Prof. Jiandong Yao at the School of Material Science & Engineering, Sun Yat-sen University. His research interests include the synthesis of high-quality two-dimensional materials by pulsed-laser deposition, the exploration of their photoelectric properties, as well as the fabrication of high-performance devices and their further applications.

Huanrong Liang

Xinyue Liu received her BS degree in Materials Physics from School of Physics Science & Engineering, Sun Yat-sen University in 2015 and her PhD degree in Condensed Matter Physics from School of Physics, Sun Yat-sen University in 2020 under the supervision of Prof. Guowei Yang. Currently, she is an Assistant Professor at the Institute of Nanophotonics, Jinan University. Her research interests include the synthesis of 2D materials and all-dielectric nanomaterials, as well as their applications in nanophotonics and working principles.

Xinyue Liu

Zhaoqiang Zheng received his BS degree in Hunan University (2011) and PhD degree in Sun Yat-sen University (2017). Then, he joined the School of Materials and Energy, Guangdong University of Technology and currently is an Associate Professor. His research interests are the design, synthesis and photodetection applications of novel 2D materials and their heterostructures.

Zhaoqiang Zheng

synergy of various atomically thin functional layers. On the whole, 2DLMs possess a variety of unique advantages in the field of photodetection, which can overcome the critical shortcomings of traditional bulk materials and bring unprecedented opportunities for the development and application of the next-generation advanced optoelectronic devices. Taking advantage of their abundant and excellent physical properties, researchers have developed various types of photodetectors based on a host of 2DLMs, including elemental semimetals/semiconductors,[33–36] post-transition metal chalcogenides,[37–41] transition metal chalcogenides,[42–51] multi-elemental 2DLMs,[52–70] as well as related van der Waals heterostructures.[19–22,27,71–87] Inspiringly, these emerging photodetectors have exhibited highly competitive device performance. For example, in 2016, Huang *et al.* achieved a remarkably high responsivity of 4.3×10^6 A W^{-1} based on a photoconductive-type black phosphorus nanosheet photodetector,[36] far exceeding those of the recently reported metal–semiconductor–metal (MSM) photodetectors built of conventional covalent semiconductors (*e.g.*, Ge (0.572 A W^{-1}),[88] GaN (4.23 A W^{-1}),[89] SiC (29 mA W^{-1}),[90] GaAs (99.01 A W^{-1})[91]). In 2019, Sun *et al.* demonstrated that a flexible MSM photodetector with monolayer MoS_2 serving as the light-sensing channel can be durable for up to 10 000 bending cycles.[51] In contrast, flexible photodetectors based on conventional covalent semiconductors commonly suffer from severe degradation after bending treatments (*e.g.*, a degeneration of 56% in photocurrent over 100 bending cycles for a CdS_xSe_{1-x} MSM photodetector).[92] In 2022, Zeng *et al.*[93] revealed that the response time of a MoS_2/WSe_2 heterojunction was down to 4 ps, which was substantially shorter than those of Ge/Si (≈ 850 ps)[94] and InP/ZnO (≈ 5.8 ns)[95] photodiodes. In another study, Schall *et al.* demonstrated a >76 gigahertz (GHz) MSM photodetector based on graphene,[96] which far exceeds those of state-of-the-art MSM photodetectors built of conventional semiconductors (*e.g.*, Si (7.5 GHz),[97] GeSn (1.26 GHz),[98] InGaAs

(2.03 GHz)[99]). Similarly, Flöry *et al.* reported a graphene/ $MoTe_2$ heterojunction photodetector with a bandwidth up to 50 GHz,[100] which was also superior to many of the previous heterojunction photodetectors such as Si/Ge (40 GHz),[101] Ge/GaAs (9.3 GHz),[102] and InGaAs/InP (3 GHz).[103]

Taking advantage of the fascinating properties, in recent years, researchers have explored a series of emerging optoelectronic applications by using these 2DLM photodetectors as the core functional components. For example, in 2019, Polat *et al.* successfully exploited a hybrid PbS quantum dots/graphene photodetector for wearable fitness monitoring spanning heart rate, arterial oxygen saturation, and respiratory rate.[104] In 2022, Lu *et al.* reported on multiplexing optical communications based on an $O–WS_2/WS_2$ photodetector by using the polarization state and the light intensity as independent transmission channels.[105] Most recently, Gao *et al.* constructed a transparent ZnO/MoS_2 photodetector array and harnessed it for an electronic eye consolidating double-sided imaging capabilities.[106] These advancements all demonstrate the enormous advantages of 2DLMs in the next-generation optoelectronic industry.

Despite significant progress, these research works are relatively fragmented. Thus far, in spite of the appearance of numerous reviews/tutorials/perspectives regarding 2DLM photodetectors, these literature reports have been largely focused on the materials, devices, effective spectrum, and performance optimization.[107–120] Some researchers have recently paid attention to the downstream applications but only focused on a relatively small domain such as infrared imaging.[121] To date, to our knowledge, there is still no systematical review regarding the extensive downstream applications of 2DLM photodetectors. This seriously prevents researchers from having a quick, timely, and comprehensive inspection of this fascinating domain and also prevents the further advancement of 2DLM optoelectronic devices from fundamental research to practical production and commercialization. In response to this, in the current review, the emerging downstream applications of 2DLM photodetectors in extensive fields, including imaging, health monitoring, target tracking, optoelectronic logic operation, ultraviolet monitoring, optical communications, automatic driving, and acoustic signal detection, have been systematically summarized, with the focus on the underlying principles. In the end, the ongoing challenges of this rapidly progressing domain have been summarized, and the potential schemes to address them have been envisioned, which aim at navigating the future exploration as well as fully exerting the pivotal role of 2DLMs towards the practical optoelectronic industry.

2. Photoelectric imaging

Optoelectronic imaging is a powerful technology that capitalizes on optoelectronic systems to obtain image information. Basically, it converts the reflected/transmitted light signals from the target into electrical signals, which are then processed to reproduce the morphology of the target in the form of

Jiandong Yao

Jiandong Yao received his BS degree in Materials Physics in 2013 from School of Physics Science & Engineering, Sun Yat-sen University and his PhD degree in Condensed Matter Physics in 2018 from School of Physics, Sun Yat-sen University under the supervision of Prof. Guowei Yang. Then, he joined the School of Materials Science & Engineering, Nanyang Technological University as a Research Fellow. Currently, he is an Associate Professor in School of Materials Science & Engineering, Sun Yat-sen University. His research interests include the controllable synthesis of low-dimensional materials and their application in optoelectronics.

images. Photoelectric imaging technology is of great significance to the breakthrough and extension of human visual ability in terms of sensitivity, spatial resolution, response rate, effective spectral domain, *etc.* Thus far, optoelectronic imaging technology has entered both civilian and military fields such as photography, medical diagnosis, security monitoring, aerospace, remote sensing, and national defense.

Currently, the traditional optoelectronic materials and devices still face a series of insurmountable challenges in imaging applications, including large device volume, low integration level, large weight, narrow effective bandwidth, slow response speed, and strict operating conditions. In recent years, 2DLMs have emerged as promising candidates to take the place of traditional optoelectronic materials. These competitors have excellent electrical and optoelectronic properties, such as high carrier mobility, tunable bandgap, excellent immunity to the short-channel effects, and outstanding light absorption ability. Most notably, the surface of 2DLMs is free of dangling bonds, making it flexible for integration of 2DLMs with complementary properties to achieve ground-breaking performance beyond individuals. These fascinating characteristics have provided 2DLMs with extremely high application value in next-generation optoelectronic imaging applications.

As an example, in 2023, Yi and collaborators constructed a SnS_2/MoS_2 van der Waals heterostructure photodetector (Fig. 1(a)) and exploited it for a visible imaging application.[27] As shown in Fig. 1(b), on account of the distinct bandgap values (≈ 1.75 eV for MoS_2 and ≈ 1.96 eV for SnS_2), the photoresponse of SnS_2 and MoS_2 is well complementary, enabling the SnS_2/MoS_2 heterojunction to realize high-performance photosensitivity across a broad visible spectral range. This is understandable since the photoresponse of the SnS_2/MoS_2 heterojunction photodetector comes from the contributions of both constituent components. In addition, the SnS_2/MoS_2 heterojunction photodetector exhibits a good reversible photoresponse to the periodic illumination, simultaneously hosting relatively low dark current, large photocurrent, and high on/off ratio (Fig. 1(c)). Furthermore, the rise/decay time is as short as 1.38/0.6 ms. The comprehensive properties make the SnS_2/MoS_2 heterojunction photodetector highly amenable to visible imaging application. On this basis, the device has been further used as the light-sensing unit in a single-pixel imaging application. As shown in Fig. 1(d), in principle, the light illuminating onto a target will be partially blocked, and the transmitted portion is detected by the SnS_2/MoS_2 heterojunction photodetector. As a consequence, the outline of the target can be obtained by the photocurrent distribution information. Fig. 1(e) shows the photocurrent mapping images extracted by the SnS_2/MoS_2 heterojunction photodetector upon red, green, and blue violet light illuminations. Distinct profiles of "SYSU" with relatively sharp margin have been successfully obtained, demonstrating the excellent imaging capability. Thus far, photodetectors built of various 2DLMs and related heterostructures, such as PbI_2,[122] $CuInP_2Se_6$,[123] WS_2/GaN,[124] $(PEA)_2PbI_4/SnP_2S_6$,[55] $1T'$-$MoTe_2/GaN$,[125] $PbI_2/InGaO$,[126] and In_2O_3/PbI_2,[127] have been developed for ultraviolet to visible

imaging application, attesting to the prodigious potency of 2DLMs in the imaging field.

Despite encouraging research advances, the aforementioned studies still face a key challenge of relatively narrow effective spectral range. Compared to ultraviolet and visible light, infrared light has a more excellent penetration ability due to the long wavelength, and it is thus less susceptible to the environmental interference such as haze and smoke. Therefore, in theory, infrared optoelectronic imaging technology possesses a strong anti-interference ability and can be potentially applied in harsh working environments. In addition, due to the benefit of infrared optoelectronic imaging technology being able to utilize the infrared radiation emitted by the targets themselves (any object above 0 K will emit infrared light) for imaging, it theoretically does not rely on external light sources and can thus work normally at night or under weak-light conditions, with excellent night vision ability. On the basis of the above background, exploring new infrared imaging systems based on 2DLMs is an attractive research topic.

As an example, most recently, Zhang *et al.* have constructed a $Ta_2NiSe_5/MoTe_2/Gr$ van der Waals heterostructure photodetector (Fig. 1(f)) and harnessed this device for ultra-broadband photoelectric imaging application.[128] In this device, the top small-bandgap Ta_2NiSe_5 layer and the middle moderate-bandgap $MoTe_2$ layer serve as light-absorbing layers and form a heterojunction with a built-in electric field facilitating spatial separation of photocarriers, while the bottom graphene layer enables high-efficiency carrier collection. Benefiting from the relatively small bandgap value of Ta_2NiSe_5, the $Ta_2NiSe_5/MoTe_2/Gr$ device demonstrates a broadband photoresponse across 520 to 2200 nm. Specifically, upon 2200 nm illumination under room temperature, the device realizes a high responsivity of 5.79 A W^{-1} and an excellent detectivity of 10^{10} Jones. By exploiting the $Ta_2NiSe_5/MoTe_2/graphene$ heterostructure photodetector as the sensing pixel, visible to near-infrared photoelectric imaging has been demonstrated by accurately reproducing the "GDUT" pattern with clear and distinct boundaries separating the pattern from the background (Fig. 1(g) and (h)). Of note, the effective spectral range of the heterostructured device far exceeds those of human vision (≈ 400–760 nm) and commercial Si-based devices (< 1100 nm), thereby manifesting intriguing prospects for future visual systems. Similarly, Zeng *et al.* fabricated $PtTe_2/Si$ heterojunction photodetectors and demonstrated room-temperature visible to far-infrared imaging.[130] On the whole, these studies depict a flexible way to achieve infrared imaging by integrating 2DLMs with small bandgap values or gapless band structures. To date, infrared imaging has been realized based on a wealth of 2DLM based photodetectors, including graphene,[131] black phosphorus,[132] black phosphorus/MoS_2,[133] $PdSe_2/Si$,[134] graphene/$PdSe_2/Ge$,[135] $PtSe_2/Bi_2Te_3/Si$,[136] *etc.*

Defect engineering is an effective means of regulating the band structure of low-dimensional materials by tailoring their defects. Therefore, apart from integrating small-bandgap 2DLMs, defect engineering is also one of the potential approaches to realize broadband optoelectronic imaging. In
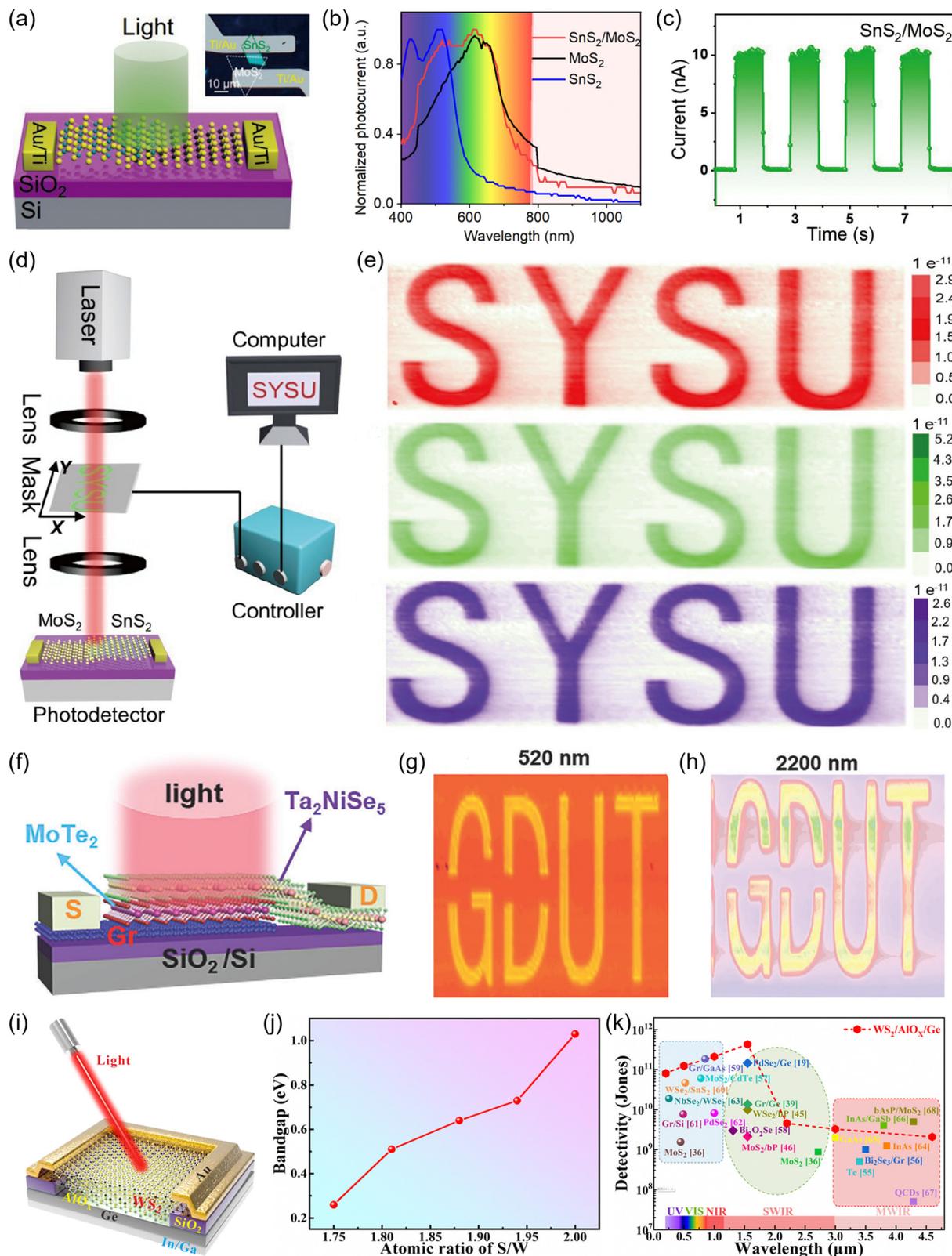
Fig. 1 (a) Schematic diagram of a SnS_2/MoS_2 heterojunction photodetector. The inset presents an optical microscopy image. (b) Spectral photoresponse of the SnS_2, MoS_2, and SnS_2/MoS_2 heterojunction photodetectors. (c) Photoswitching curve upon periodic 520 nm illumination. (d) Schematic illustration of the experimental configuration for the single-pixel photoelectric imaging. (e) The imaging profiles for an ''SYSU'' pattern by using 671 (red), 532 (green), and 405 nm (blue-violet) light as the light source. Reproduced from ref. 27 with permission from Science China Press, copyright 2023. (f) Schematic diagram of a $Ta_2NiSe_5/MoTe_2$/graphene heterojunction photodetector. (g) and (h) The imaging profiles of a ''GDUT'' pattern by using 520 (green) and 2200 nm (infrared) light as the light source. Reproduced from ref. 128 with permission from John Wiley and Sons, Inc., copyright 2024.

(i) Schematic diagram of a WS$_{2-x}$/AlO$_x$/Ge heterojunction photodetector. (j) Bandgap value as a function of the S/W ratio of WS$_{2-x}$. (k) A summary of the detectivity values of the WS$_{2-x}$/AlO$_x$/Ge heterojunction photodetector under various wavelengths. The detectivity values of other reported 2DLM based devices have also been provided for comparison. Reproduced from ref. 129 with permission from American Chemical Society, copyright 2021.

2021, Wu *et al.* constructed an ultra-broadband photodetector built of S-deficient WS$_2$ (WS$_{2-x}$), an AlO$_x$ interfacial passivation layer, and Ge (Fig. 1(i)).[129] As shown in Fig. 1(j), the bandgap value of WS$_2$ decreases monotonously with increasing sulfur vacancies. Specifically, the estimated bandgap of WS$_{2-x}$ reaches 0.51/0.26 eV for an *x* value of 0.19/0.25, corresponding to the absorption edge of 2437/4781 nm. On account of the narrow bandgap of WS$_{2-x}$ induced by the vacancy defects, the WS$_{2-x}$/AlO$_x$/Ge device demonstrates a room-temperature ultra-wide spectral photoresponse spanning from deep ultraviolet (200 nm) to mid-wave infrared (MWIR, 4.6 μm) (Fig. 1(k)). As a consequence, by using the WS$_{2-x}$/AlO$_x$/Ge heterojunction photodetector as the light-sensing unit, mid-infrared imaging for the "LIGHT" pattern at 4.6 μm has been realized. As a demonstration of the practical application value of infrared imaging, Yu *et al.* have recently exploited S-deficient ZrS$_3$ infrared photodetectors for imaging a heating tube behind a silicon wafer.[48] It was determined that the invisible heating tube can be precisely identified by the eye using the S-deficient ZrS$_3$ infrared photodetector, demonstrating the great potential for non-invasive inspection.

Terahertz waves represent electromagnetic radiation that lies between microwave and infrared light, with unique physical characteristics, making terahertz detection have significant

advantages in a variety of fields. For example, the high-resolution characteristics of terahertz waves enable a terahertz radar to detect smaller targets or provide more accurate positioning compared to traditional low-frequency radar. In addition, compared to ultraviolet, visible, and infrared light, terahertz waves have stronger penetration capabilities and can thus efficiently, conveniently, and non-destructively detect hidden explosives, weapons, and other prohibited items. Therefore, terahertz detection has become an important research field. 2D topological semimetals, including Weyl and Dirac semimetals, have raised broad research enthusiasm on account of their special energy band structure containing a Weyl/Dirac cone, which provides these materials with an unlimited light absorption range. As a consequence, these building blocks exhibit great potency in the field of terahertz detection and imaging.

As an example, in 2020, Guo *et al.* successfully demonstrated a terahertz photodetector based on the type II topological semimetal PdTe$_2$ (0.04–0.3 THz) and successfully harnessed this device for imaging application.[137] As shown in Fig. 2(a), the device is composed of a PdTe$_2$ flake as well as symmetrically distributed drain and source electrodes. It exhibits a stable and rapid photoresponse in the frequency range of 0.04–0.3 THz (Fig. 2(b)), showing the tremendous potential for broadband
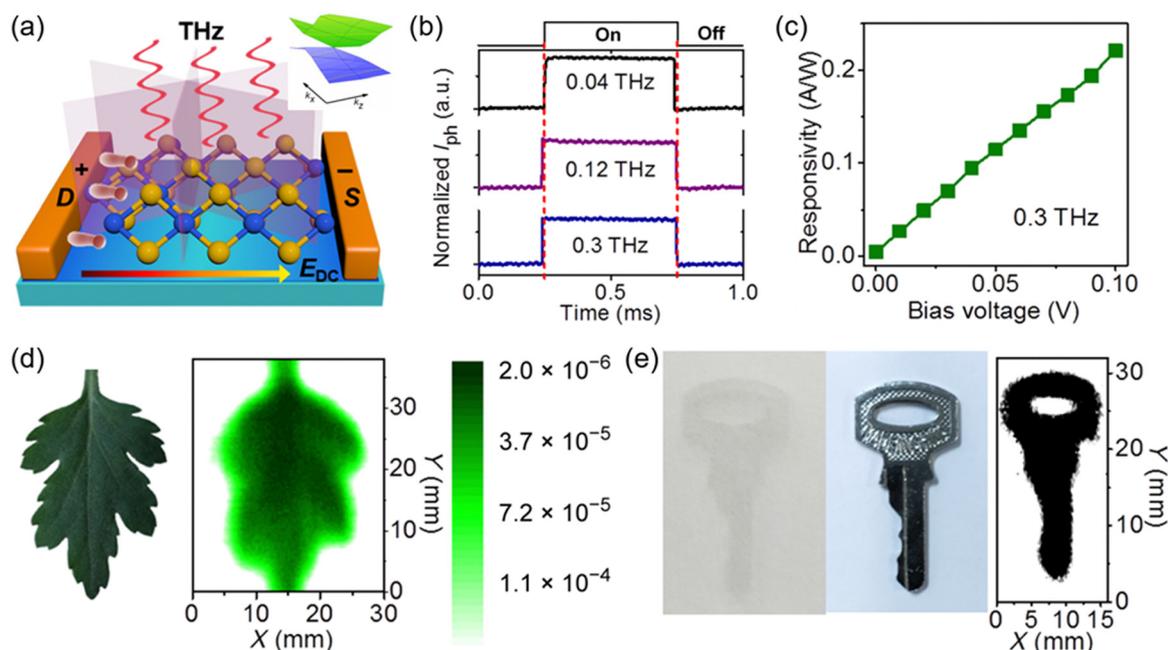
Fig. 2 (a) Schematic illustration of the device structure of the PdTe$_2$ photodetector in the biased mode. The inset shows the projection of the Dirac cone along the k_x–k_z plane. (b) Typical photoswitching curves of the PdTe$_2$-based device under illumination with different photon frequencies. (c) Responsivity as a function of bias voltage upon 0.3 THz illumination. (d) and (e) Results of terahertz imaging for a fresh leaf (0.12 THz) and a hidden key (0.3 THz) by using the PdTe$_2$ photodetector as the sensing pixel. Reproduced from ref. 137 with permission from American Association for the Advancement of Science, copyright 2020.

detection. This benefits from the gapless band structure (inset of Fig. 2(a)). As shown in Fig. 2(c), the photoresponse increases linearly with increasing bias voltage. This is because the bias voltage can break the symmetrical plane, making the none-quilibrium carriers move laterally along the electric field. Benefiting from the fast and stable photoresponse, the $PdTe_2$ device is further developed for terahertz imaging application. Fig. 2(d) presents the imaging result for a fresh leaf. The distribution of veins can be clearly identified, which is reasonable as water exhibits strong absorption of terahertz waves. Similarly, the profile of a key can also be well extracted by terahertz imaging (Fig. 2(e)), as metal manifests a strong shielding effect for terahertz waves.

Thus far, in addition to $PdTe_2$, a series of topological 2D van der Waals materials and related heterostructures, including graphene,[138] Bi_2Se_3,[139] $Bi_2Te_{2.2}Se_{0.8}$,[140] $PtTe_2$,[141] $MnBi_2Te_4$,[142] $NbIrTe_4$,[143] $1T\text{-}CoTe_2$,[144] $ZrGeSe$,[145] $MnBi_2Te_4$/graphene,[146] $NiTe_2$/graphene,[147] and $NbIrTe_4$/graphene,[148] have been harnessed for terahertz sensing. However, in the current stage, there are still some critical issues to be addressed. Firstly, the photosensitivity of the state-of-the-art 2D topological material based terahertz photodetectors still needs to be further improved. In previous studies, due to the relatively high electrical conductivity of semimetallic materials, these devices typically suffer from severe background noise, thereby requiring lock-in amplifiers or low operating temperatures to assist in reading out the photocurrent signals. This will significantly increase the volume, complexity, weight, and cost of the optoelectronic systems, while reducing their portability and integratability in practical applications. Secondly, the vast majority of 2D topological material based terahertz optoelectronic devices have been produced based on cumbersome mechanical exfoliation and stacking techniques.[138,139,141] Nevertheless, the device yield of these preparation techniques is quite low. In addition, the lateral size of the exfoliated 2DLMs is substantially limited ($\approx$ tens of micrometers), which curtails their further application in integrated chips demanding arrayed devices. Therefore, it is challenging for these building blocks to meet the needs of practical applications. Finally, many previously studied 2D topological materials, such as $PdTe_2$, $PtTe_2$, $TaIrTe_4$, $NbIrTe_4$, *etc.*, suffer from issues such as complex crystal structures, environmentally unfriendly compositions, low crust reserves, or high material costs, which are not conducive to large-scale commercial applications.

Despite significant research progress, most of the preceding optoelectronic imaging applications have been based on single-pixel modes, which is highly inefficient as the signals have to be extracted in a step-by-step way. As for practical applications, it is often necessary to construct device arrays with small device-to-device variation to significantly improve the efficiency of optoelectronic imaging. As a rule, the key difficulty in preparing device arrays is to achieve scalable preparation of high-quality 2DLMs.

In response to the above predicament, in 2020, Zeng *et al.* developed a simple two-step growth process to achieve large-scale preparation of 2DLMs.[130] As shown in Fig. 3(a), a large-area Pt nanofilm is firstly deposited on the substrate using a magnetron sputtering method. Then, by tellurizing the Pt nanofilm at a relatively high temperature, a large-area $PtTe_2$ nanofilm can thus be obtained. Inspiringly, this technique allows the direct synthesis of a 2D $PtTe_2$ layer on a 2-inch substrate. As shown in Fig. 3(b), $PtTe_2$ nanofilms with different thicknesses can be flexibly prepared by controlling the thickness of the original Pt nanofilms. By combining photolithography technology, arrayed Si windows can be produced by selectively etching away the oxide layer of the SiO_2/Si substrate, and $PtTe_2$ nanofilm is subsequently deposited on them to prepare a 4×4 $PtTe_2$/Si heterojunction photodetector array and graphene layer is transferred atop to serve as the charge collecting electrode (Fig. 3(c) and (d)). The $PtTe_2$/Si devices exhibit an ultrabroadband photoresponse from ultraviolet to far-infrared (Fig. 3(e)), benefiting from the ultra-wide light absorption of $PtTe_2$ enabled by the gapless band structure (Fig. 3(f)). On this basis, the $PtTe_2$/Si heterojunction photodetector array has been successfully used as the sensing pixels to achieve ultrabroadband multi-pixel optoelectronic imaging applications (Fig. 3(g)). On the whole, this study provides a convenient route to prepare large-area continuous 2DLM nanofilms. In 2023, by tellurizing a pre-deposited Mo nanofilm, Wu *et al.* achieved the wafer-scale preparation of $1T'\text{-}MoTe_2$ nanofilm.[149] Similarly, an 8×8 $1T'\text{-}MoTe_2$/Si heterojunction photodetector array has been fabricated and multi-pixel imaging for a "heart" pattern has been realized. In another study, by depositing a Pt nanofilm and performing post-selenization treatment, Ye *et al.* achieved the preparation of centimeter-scale $PtSe_2$ nanofilms.[150] On this basis, a 9×9 $PtSe_2$/Si heterojunction photodetector array has been constructed and multi-pixel imaging for the "Z", "J", and "U" patterns has been realized.

To date, in addition to the two-step growth method mentioned above, researchers have also developed other techniques, such as molecular beam epitaxy (MBE),[151,152] pulsed-laser deposition (PLD),[153,154] and metal–organic chemical vapor deposition (MOCVD),[155] to achieve large-scale growth of continuous 2DLMs. These techniques lay a solid foundation for the implementation of multi-pixel optoelectronic imaging application. In the upcoming future, more advancements on multi-pixel optoelectronic imaging can be expected.

Despite the remarkable research progress, most of the 2DLM based optoelectronic imaging research has been based on rigid optoelectronic devices, which greatly limits their practical application scopes. Compared to rigid devices, flexible optoelectronic imaging devices have a series of outstanding advantages. Firstly, flexible optoelectronic imaging devices have excellent bending, twisting and folding capabilities, which enable them to adapt to various complex surfaces. In contrast, it is cumbersome for the rigid optoelectronic imaging devices to adapt to diverse application environments due to their fixed shape. Secondly, flexible optoelectronic imaging devices are usually lighter and thinner than the rigid ones, which makes them more portable. As a result, these devices have extremely high application value in fields requiring strict weight control, such as aerospace and wearable devices. Furthermore, upon
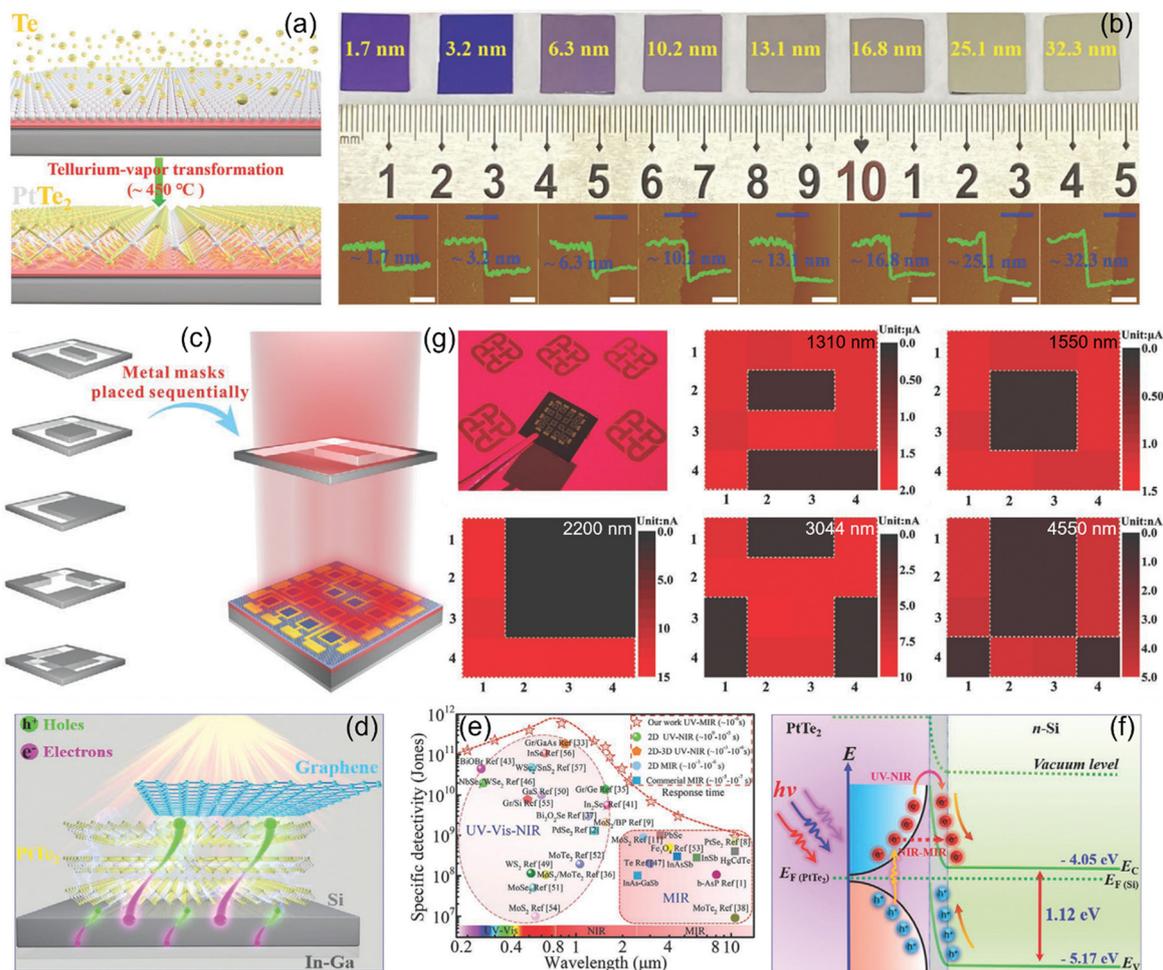
Fig. 3 (a) Schematic illustration of the preparation process for producing large-scale PtTe$_2$. (b) Digital photographs and AFM thickness profiles of the PtTe$_2$ nanofilms of different thicknesses. (c) Schematic illustration of the optoelectronic imaging based on an array of PtTe$_2$/Si heterojunction photodetectors. (d) Schematic diagram of the device structure. (e) Spectral photoresponse. (f) Energy band diagram illustrating the working mechanism. (g) Photocurrent mapping images upon 1310 ("P"), 1550 ("O"), 2200 ("L"), 3044 ("Y"), and 4550 ("U") nm illuminations, respectively. Reproduced from ref. 130 with permission from John Wiley and Sons, Inc., copyright 2020.

external shocks, flexible optoelectronic imaging devices can better buffer external forces through deformation, thus exhibiting better shock resistance. Most importantly, flexible optoelectronic imaging devices can better match different illumination conditions and imaging targets through deformation, providing an additional modulation degree for improving the imaging quality. However, thus far, the research regarding the optoelectronic imaging system of flexible 2DLM photodetectors is still rather limited, predominantly due to the lack of low-temperature synthesis technology for preparing 2DLMs, whereas most flexible substrates are not resistant to high temperature. As such, most flexible 2DLM photodetectors have been fabricated based on manual transfer techniques,[156–159] which is impractical for actual applications.

To address this issue, in 2023, Gao *et al.* developed a spray coating technique for the construction of flexible hybrid MoS$_2$/ZnO photodetectors and successfully exploited them for electronic eyes.[106] Specifically, the MoS$_2$ nanosheets are produced using an intercalation-based ultrasonic exfoliation technique.

Then, they are composited with ZnO nanoparticles and used for spray coating on flexible transparent poly(vinylalcohol) substrates with prepatterned Ag electrodes (Fig. 4(a)). As shown in Fig. 4(b), the MoS$_2$/ZnO device is well reproducible and has a fast photoresponse. The rise/decay time is as short as 100/250 ms, which can meet the high-speed data acquisition requirements. Therefore, the devices have been further harnessed for e-eye application (Fig. 4(c)). Compared to conventional rigid imagers, the bendable imager can adapt its photosensing area into a curved surface to match the field curvature (Fig. 4(d)). As a consequence, the photocurrent of each imaging pixel can be optimized for image reconstruction, and the imaging for the "E" (Fig. 4(e)) and cross shape (Fig. 4(f)) patterns have been realized. Moreover, with the advantage of the high transparency, imaging from the back side illumination has been demonstrated (Fig. 4(g)), functioning as the insect compound eyes.

In sum, this study provides a unique pathway for the economical and high-efficiency preparation of 2DLM based
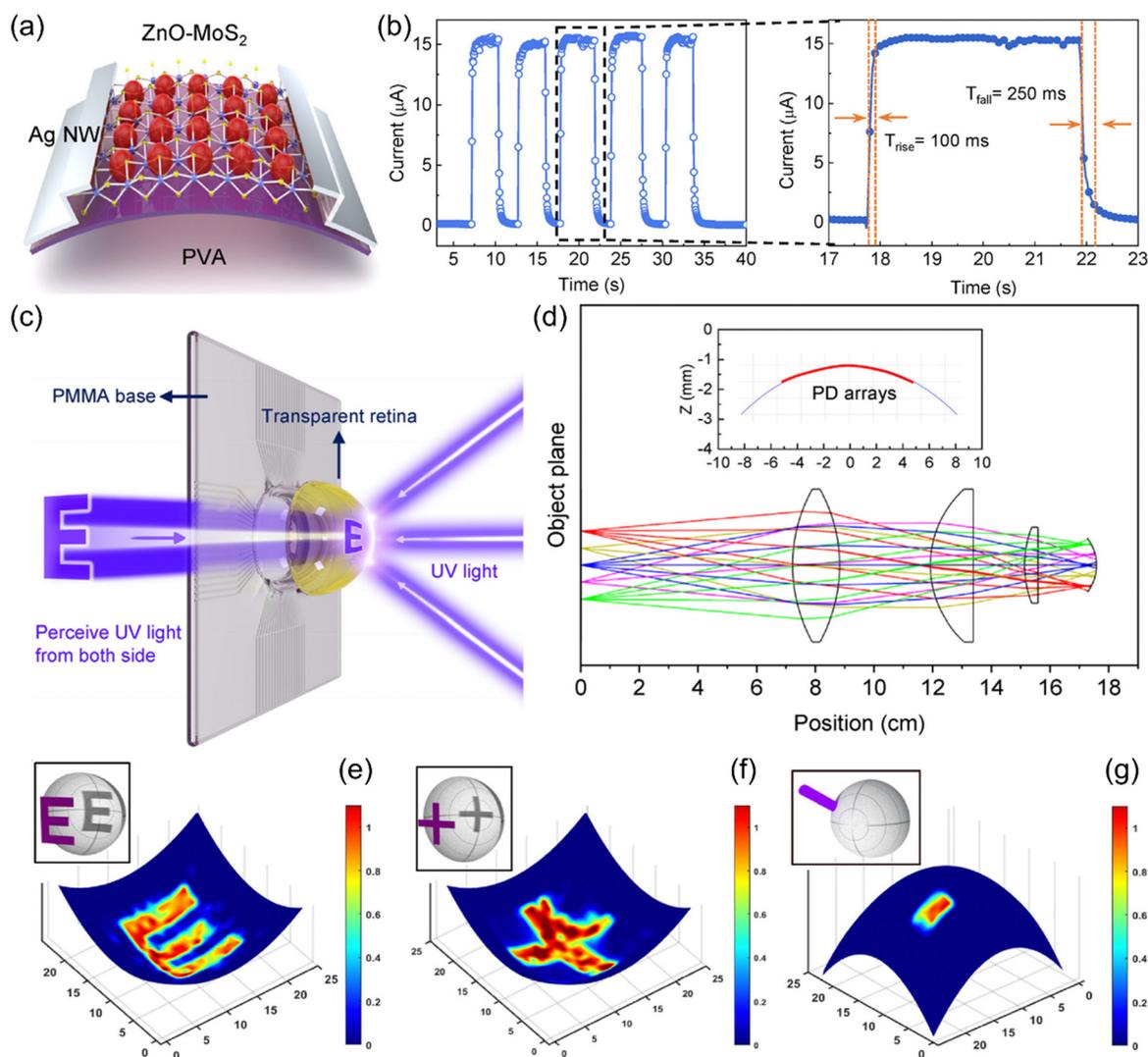
Fig. 4 (a) Schematic diagram of a flexible MoS$_2$/ZnO photodetector. (b) Photoswitching curve (left) and an enlarged photoswitching cycle (right). (c) Schematic illustration of an e-eye system based on the flexible MoS$_2$/ZnO photodetectors. (d) Ray-tracing simulation of the lens set-up. Inset: The matched curvature of the photodetector array with the focal plane. (e) and (f) Reconstructed images of the letter "E" and cross shape based on an electronic eye with forward illumination. (g) Reconstructed image of one point based on an electronic eye with backward illumination. Reproduced from ref. 106 with permission from Elsevier, copyright 2023.

flexible optoelectronic imaging systems. However, in the current stage, it still suffers from some critical issues. On one hand, although the liquid phase exfoliation technology can be performed at room temperature, the produced photosensitive materials usually suffer from high defect density and interfacial contamination, which seriously plagues the further improvement of device properties. On the other hand, the thin films deposited by spray coating technology are commonly relatively loose, and the long-range stability of the corresponding devices still needs further improvement.

On consideration of these tangible challenges, in recent years, researchers have been devoted to exploring the potential technologies for low-temperature *in situ* synthesis of 2DLMs directly on flexible substrates.[160–164] As an example, in 2017, Zheng *et al.* demonstrated the direct synthesis of the

Mo$_{0.5}$W$_{0.5}$Se$_2$ nanofilms on polyimide (PI) substrates by using PLD.[161] The low-temperate synthesis probably benefits from the energetic species enabled by the high-energy focused pulsed laser beam. Importantly, the PLD-derived photodetector exhibits a largely unchanged photoresponse over 100 bending cycles. In addition, the growth conditions also play a critical role in the deposition temperature. For example, in 2017, Gong *et al.* achieved the low-temperature synthesis of MoS$_2$ by optimizing the reaction precursors.[162] In this study, $(NH_4)_2MoO_4$ is used as the Mo source and the deposition temperature is lowered to 450 °C. The mechanism for low-temperature synthesis can be well explained as follows. In the thermodynamic viewpoint, the decomposition of $(NH_4)_2MoO_4$ to MoO_3, H_2O, and NH_3 can lower the system's overall energy. From the dynamic viewpoint, the MoO_3 species from the

decomposed $(NH_4)_2MoO_4$ is more energetic than the MoO_3 powder. In addition, the gas produced during the decomposition process can bring the MoO_3 molecule out to enable more efficient reaction. As a consequence, the reaction is thermodynamically and kinetically favored. In 2023, Zhang *et al.* achieved the synthesis of $PtSe_2$ under merely 200 °C by using a plasma-assisted selenization process.[164] In principle, the bombardment of Ar plasma can efficiently ionize Se atoms to produce active Se radicals with high chemical reactivity, which is conducive to transforming the Pt nanofilm into the $PtSe_2$ nanofilm. In summary, the above technologies provide highly promising means for the future preparation of high sensitivity flexible optoelectronic imaging systems.

While conventional imaging techniques are highly effective in many situations, in certain specific applications, polarization imaging offers more valuable information and solutions, thus it has been the subject of intensive research. By merging the spatial, spectral, and polarization information of targets, polarization imaging technology not only increases the amount of information obtained from the targets but also enhances the detection capability. With the expanding application scope of polarization imaging in fields such as agriculture, medicine, engineering, atmospheric science, and astronomy, it certainly

exhibits broad application prospects in the future. With the requirements for miniaturization and flexibility, 2DLMs offer an important avenue. These materials demonstrate outstanding inherent advantages in being easily integrated into micro/nano optoelectronic devices/systems. Moreover, the high in-plane anisotropy of the crystal structures of a wealth of 2DLMs, including black phosphorus,[165] violet phosphorus,[166] AsP,[167] SiP,[168] ReS_2,[169] $ReSe_2$,[170] and PdPSe,[171] results in intrinsically anisotropic optical properties. As a consequence, the necessity for integrated optical components has been exempted by constructing polarized photodetectors built of these 2DLMs, reducing simultaneously the processing complexity, volume, and cost.

In 2023, Kong *et al.* demonstrated contrast-enhanced polarization imaging under scattering illumination based on a 1T′ $MoTe_2/MoS_2$ van der Waals heterojunction photodetector (Fig. 5(a)).[172] As shown in Fig. 5(b) and (c), the crystal structure of 1T′ $MoTe_2$ exhibits strong in-plane anisotropy. As a consequence, the $MoTe_2/MoS_2$ heterojunction device demonstrates pronounced polarization-discriminating photosensitivity. Specifically, the anisotropic ratios are calculated to be 1.77, 1.98, 1.83, and 2.07 upon 852, 915, 1300, and 1550 nm illuminations, respectively. In this study, the $MoTe_2/MoS_2$ photodetector is
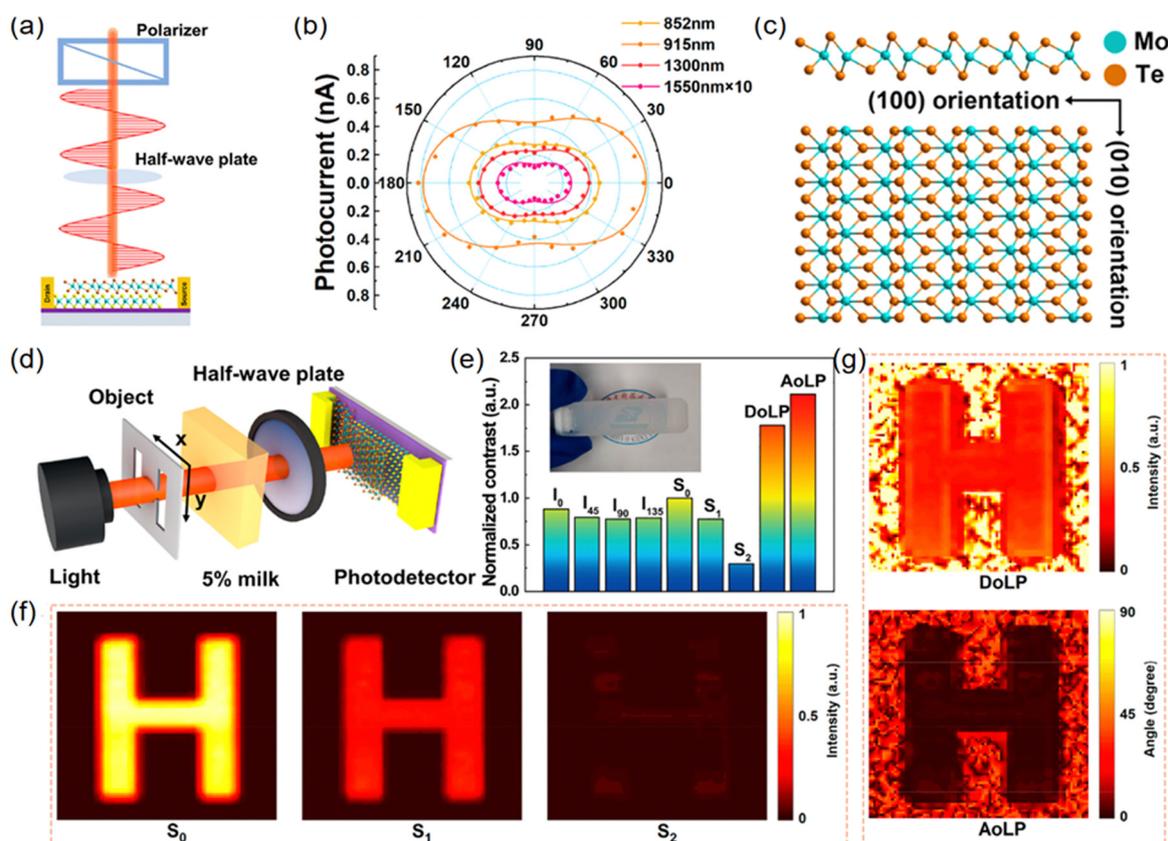
Fig. 5 (a) Schematic diagram of polarization detection based on a $MoTe_2/MoS_2$ photodetector. (b) Polar plots depicting the photocurrent as a function of polarization angle under 852, 915, 1300, and 1550 nm illuminations. (c) Schematic diagrams of the side view (top) and top view (bottom) of 1T′ phase $MoTe_2$. (d) Schematic of the polarization imaging system in a scattering environment. (e) A summary of the normalized imaging contrast values of various parameters. (f) The imaging results of S_0, S_1, and S_2 under 915 nm light illumination. (g) The imaging results of DoLP and AoLP. Reproduced from ref. 172 with permission from American Chemical Society, copyright 2023.

used as a single-pixel imaging sensor and the scattering medium consists of a water solution with 5% volume of milk (Fig. 5(d)). To improve the contrast of imaging results in a scattering environment, traditional light intensity parameters are replaced by a polarization parameter. In theory, the polarization state of an electromagnetic wave can be described using the Stokes vector. The Stokes vector is a 4D vector and can be defined as:

$$S(x,y) = \begin{bmatrix} S_0(x,y) \\ S_1(x,y) \\ S_2(x,y) \\ S_3(x,y) \end{bmatrix} = \begin{bmatrix} I_{0°}(x,y) + I_{90°}(x,y) \\ I_{0°}(x,y) - I_{90°}(x,y) \\ I_{45°}(x,y) - I_{135°}(x,y) \\ I_R(x,y) - I_L(x,y) \end{bmatrix},$$

where $I_{0°}(x,y)$, $I_{90°}(x,y)$, $I_{45°}(x,y)$, and $I_{135°}(x,y)$ represent the intensity of polarized light along corresponding directions, $I_R(x,y)$ and $I_L(x,y)$ represent the intensity of right circular and left circular polarized light, S_0 refers to the total intensity of light, which is the intensity sum of all polarization directions and corresponds to non-polarized light. S_1 and S_2 describe the information about the polarization direction of light. S_3 describes the information about the rotation direction of the light vector. Obviously, for linear polarization imaging, the information contained in S_0, S_1, and S_2 is essential. In addition, the degree of linear polarization (DoLP) and angle of linear polarization (AoLP) are utilized in the signal processing procedure, which can be calculated from the Stokes vector. The DoLP and AoLP can be defined using the following equations:

$$\text{DoLP} = \frac{\sqrt{S_1^2(x,y) + S_2^2(x,y)}}{S_0(x,y)},$$

$$\text{AoLP} = \frac{1}{2}\arctan\left(\frac{S_2}{S_1}\right),$$

As shown in Fig. 5(e), the contrast ratio of the output images under various parameters is calculated using the 8-neighbors contrast calculation method and the corresponding imaging results are depicted in Fig. 5(f) and (g). Significantly, the contrast ratios of DoLP and AoLP are 78% and 112% higher than S_0, demonstrating that the device has potential for enhanced-contrast polarization imaging. Overall, this study depicts an avenue for increasing the imaging quality based on anisotropic 2DLMs.

In the end, it is to be emphasized that the response rate of photodetectors is one of the key ingredients dominating the imaging efficiency. In the above research work by Kong et al.,[172] the response/recovery time of the MoTe$_2$/MoS$_2$ heterojunction photodetectors exceeds 100 μs, which is adverse to the rapid image acquisition. This is probably originated from the unreasonable device design. In a lateral 2DLM heterostructure, the photocarriers need to drift a long distance prior to being collected by the electrodes after these additional charges are separated by the built-in electric field. Fortunately, vertically constructed heterostructures exhibit great potency to overcome this issue.[173,174] For example, by using graphene as the top and bottom electrodes, Yan et al. prepared a vertical Gr/GaSe/InSe/Gr

heterojunction photodetector.[173] Profiting from the shortened transport path and the efficient collection of photocarriers by high-mobility graphene electrodes, the response/recovery time of the device is as short as 1.85/2.05 μs.

3. Health monitoring

Photoplethysmography (PPG), a newly emerged technique relying on photodetection, has been widely used as a non-invasive physiological signal perception technology in the wearable health monitoring field. In principle, PPG utilizes the light scattering/absorption characteristics of tissues and blood for identification of physiological signals. When the heart contracts, the amount of blood in the vessels increases, causing a change in the degree of light reflectance/absorption, finally resulting in a pulsating signal. By processing and analyzing this signal, many useful physiological parameters such as heart rate (HR), blood oxygen saturation (SpO$_2$), and respiratory rate (RR) can be extracted. When using PPG technology for physiological signal identification, photodetectors are usually placed on the skin surface to extract parameters like HR and RR. Under this working condition, the flexibility of the materials/devices is essential. If rigid materials are used, the contact between the sensor and the skin surface may be inadequate, which will lead to a decrease in signal quality. Additionally, rigid materials may make the devices less comfortable to wear and could potentially degrade their durability and reliability. Therefore, it is imperative to consider the use of flexible building blocks to achieve intimate contact quality and comfort level. In this consideration, on account of the atomic-level thickness, 2DLMs exhibit excellent mechanical properties, which enable them to be highly flexible while also possessing favorable optical and electrical characteristics.[164,175–177] As a result, these building blocks possess tremendous potential for advancing the field of wearable health monitoring industry.

In order to achieve this purpose, in 2019, Polat et al. developed a flexible graphene/PbS quantum dot (GQD) heterojunction photodetector constructed on a bendable polymer substrate and the designed prototype device successfully achieved a series of health monitoring functions (Fig. 6(a)).[104] In this study, Au/Ti electrode pads were pre-deposited on a polyethylene naphthalate (PEN)/polyethylene terephthalate (PET) film using thermal evaporation and electron-beam evaporation. Chemical vapor deposition (CVD)-grown graphene was then transferred onto the substrate using polymethyl methacrylate (PMMA). The graphene channels were further patterned using photolithography and oxygen plasma etching processes, and PbS colloidal quantum dots were subsequently spin-coated onto the graphene channels. Fig. 6(b) and (c) show the digital photographs of the GQD photodetectors constructed on the PET substrate and integrated in a bracelet, demonstrating excellent bendability, conformability, and wearability. As shown in Fig. 6(d)–(h), the GQD prototype device can be operated in two distinct modes: transmission PPG and reflectance PPG. In the reflectance mode, an LED light source is
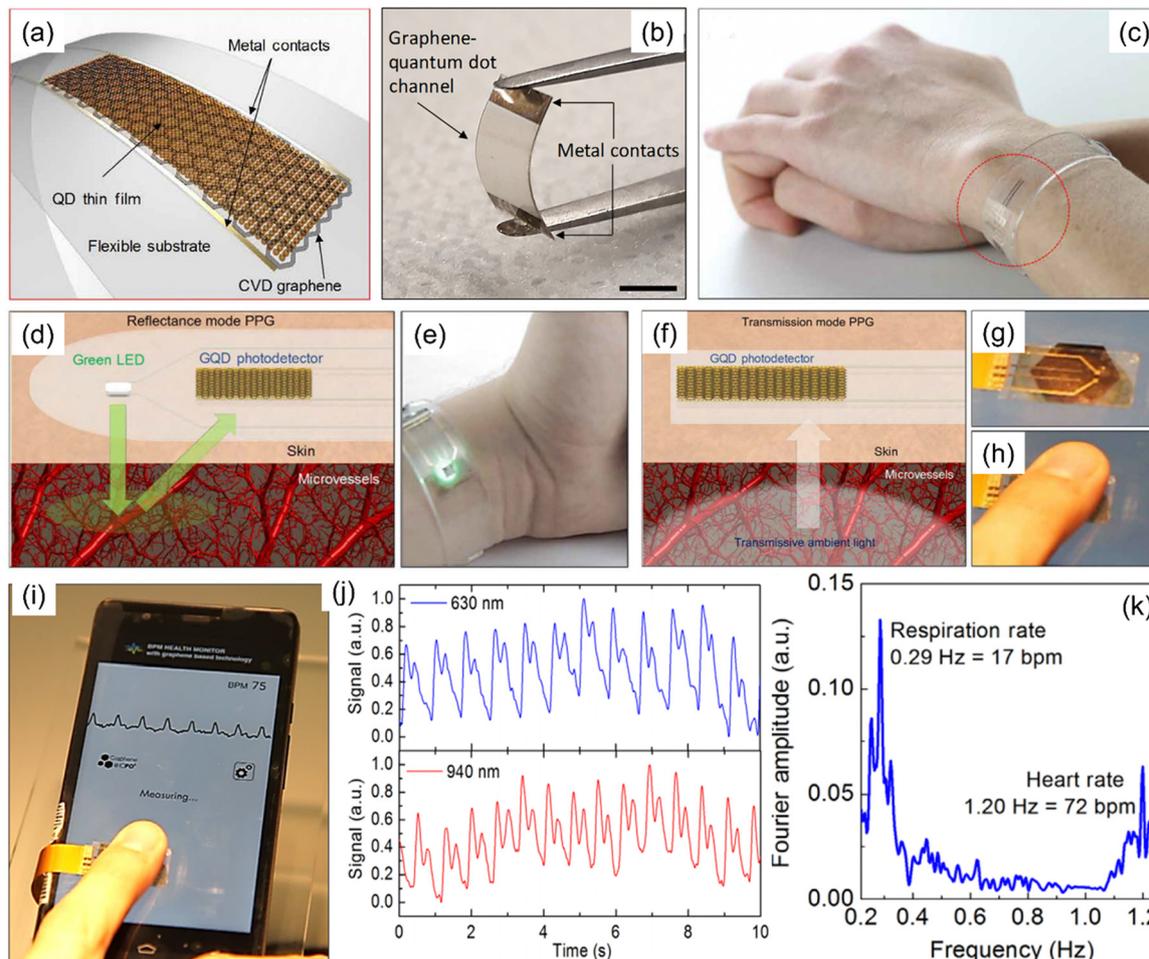
Fig. 6   Wearable health monitoring application based on flexible GQD photodetectors. (a) Schematic diagram of a GQD photodetector integrated on a flexible substrate. (b) Photograph of a GQD photodetector on a PET substrate. Scale bar: 5 mm. (c) Photograph of a wearable GQD prototype device integrated on a wristband. (d) Schematic illustration of the reflectance mode for PPG. The change in the microvascular volume leads to variation in the intensity of the reflected light signal received by the GQD photodetector. (e) Photograph of the health monitoring wristband operated in reflectance mode. (f) Schematic illustration of the transmission mode for PPG. Ambient light as the light source passes through a finger and reaches the GQD photodetector on the other side. (g) and (h) Photographs of the GQD health patch operated in transmission mode. (i) Photograph showing the real-time monitoring of the PPG based on a GQD health patch paired with a mobile phone. (j) Typical PPG results extracted under 633 nm and 940 nm illuminations, respectively. (k) Fourier transformation of a PPG reading to extract the characteristic frequencies of HR and RR. The peaks located at 0.29 Hz and 1.20 Hz indicate the RR and HR of an individual. These frequencies correspond to a breathing rate of 17 breaths per minute and a heart rate of 72 beats per minute, respectively. Reproduced from ref. 104 with permission from American Association for the Advancement of Science, copyright 2019.

integrated. After passing through the skin and interacting with the underneath tissues/blood vessels, a portion of the incident light will be reflected and identified by the GQD photodetector, and then converted into specific electrical signals, which are finally sent to an external processor for further analysis and processing. With each heartbeat, the blood vessels expand or contract in response, causing a change in their volume. This change affects the reflectance of light by the blood vessels, leading to variation in the output electrical signal of the GQD photodetector. Accordingly, analyzing the measured electrical signal can provide relevant information about blood flow. The transmission mode works in a similar principle, except that it detects the ambient light signal passing through the blood vessels/tissues underneath the skin, which is enabled by the broadband photosensitivity of the GQD photodetector. As

shown in Fig. 6(i), by wirelessly transmitting the data of a GQD photodetector to a smartphone *via* a Bluetooth module, real-time health monitoring can be realized.

Hemoglobin in erythrocyte plays an important physiological role in transporting oxygen by binding with O_2. SpO_2 serves as a vital clinical indicator for diagnosing diseases, especially hypoxemia. On account of the low absorption of red light and high absorption of infrared light, blood with high oxygenated hemoglobin levels appears distinctly bright red in color. In contrast, non-oxygenated hemoglobin commonly appears dark red, showing high absorption of red light and low absorption of infrared light. As a consequence, the difference in light absorption between oxygenated hemoglobin and non-oxygenated hemoglobin in the blood is comparatively significant at ≈ 633 nm and ≈ 940 nm (Fig. 6(j)). Consequently, the

PPG reading under these two wavelengths is extracted to measure SpO_2.

Due to the dynamic light absorption by blood and constant absorption by other biological tissues, the signal obtained from a PPG record can be divided into two parts: direct current (DC) signal and alternating current (AC) signal. The AC signal in PPG, which contains only the blood flow information, can be exploited for frequency analysis to obtain information about HR and RR by performing Fourier transformation. As shown in Fig. 6(k), the peaks at higher frequencies represent the inherent frequency of heartbeats, while the peaks at lower frequencies represent the RR manifested as a periodic modulation of heartbeats emanated from respiration. Moreover, a Bland-Altman plot analysis has been conducted by comparing this work with a clinically advanced PPG technology. A consistency correlation coefficient of 0.98 is extracted, demonstrating the high reliability of the GQD device.

Currently, in spite of the pioneering success, there is still much room for further improvement for the 2DLM photodetector-based health monitoring devices in term of accuracy, reliability, and application fields. Firstly, effectively separating the physiological signals from the environmental optical noise is still quite challenging, especially for the transmission working mode. In addition, most of the 2DLM based photodetectors suffer from a sub-linear photoresponse (*i.e.*, small linear dynamics range).[160,178] This will seriously curtail the accurate extraction of physiological information. In the future, machine learning algorithms can be exploited to improve the accuracy of signal reading. Furthermore, the linear dynamic range of 2DLM based photodetectors can be further extended through rational device design.[179] Moreover, conventional 3D metal contacts have been used as the electrodes in this study, which will suffer from severe cracks/wrinkles after repeated bending treatments, leading to degenerated photosensitivity.[180] Therefore, in the future, novel 2D electrodes such as Bi_2Te_3, VS_2, NbS_2, and $PtBi_2$ can be integrated for further improving the flexibility.[181–184] In the end, recent studies have shown that photodetectors can also be used to monitor the states of human organs, such as the extruded states.[185] Further development is needed for the application of 2DLMs in this burgeoning field.

4. Target photoelectric tracking

Micro-area target photoelectric tracking is an emerging technology that utilizes photoelectric sensors and image processing technology to identify, monitor, and track the position and motion trajectory of tiny targets in real time. This technology usually exploits high-resolution photoelectric sensors to identify the motion of targets at the microscopic scale, and extracts the features and motion parameters through image processing algorithms. Micro-area target photoelectric tracking has a series of advantages such as high spatial resolution, non-destructive monitoring, as well as high speed, and this technique thus has potential application value in a variety of

domains, including observation of microorganisms, handwriting recording, drug delivery, *etc.* In the past decade, 2DLMs have shown prominent advantages in high-speed and highly integrated optoelectronic devices due to their excellent compatibility with commercial micro/nano manufacturing techniques, ease of integration, strong light-harvesting capability, and high carrier mobility. Therefore, these newly emerged competitors have broad application prospects in the field of micro-area target photoelectric tracking. However, relevant research has still been relatively scarce in recent years.

To this end, in 2020, Luo and collaborators prepared a γ-In_2Se_3/GaAs heterojunction photodetector array (1 × 10) and successfully exploited it for the trajectory tracking of a light spot.[186] The preparation of the γ-In_2Se_3/GaAs photodetector array is achieved through patterning technique assisted magnetron sputtering deposition (Fig. 7(a)). Specifically, photolithography patterning process assisted selective-area solution etching technology is firstly used to prepare exposed GaAs windows on the Al_2O_3/GaAs substrate. Afterwards, magnetron sputtering deposition of a γ-In_2Se_3 thin film on the bare GaAs windows is carried out to construct the γ-In_2Se_3/GaAs heterojunctions. As confirmed by the sharp peaks of the X-ray diffraction pattern, the γ-In_2Se_3 nanofilm grown by magnetron sputtering exhibits relatively high crystallinity. By utilizing the photovoltaic effect, the γ-In_2Se_3/GaAs device can be operated under self-powered conditions, which greatly suppresses its dark current. Under 660 nm irradiation, the on/off ratio, responsivity, and detectivity reach 1.29×10^4, 0.25 A W^{-1}, and 7.34×10^{12} Jones, respectively. More importantly, the device demonstrates a fast response rate with a response/recovery time of 23.6/146.7 µs (Fig. 7(b)). Meanwhile, the device array exhibits high uniformity with reliable device-to-device variation (Fig. 7(c)). The preceding characteristics have jointly provided the γ-In_2Se_3/GaAs heterojunction photodetector array with tremendous potential for application in micro-area target photoelectric tracking. The researchers have used this photodetector array for real-time tracking of a moving light spot. As shown in Fig. 7(d) and (e), the arrayed γ-In_2Se_3/GaAs sensing units respond sequentially to the light simulation, verifying their target motion tracking function.

Due to the linear arrangement of the photoelectric sensor array in the above study, it can only be used to track the linear motion of the target. To address this deficiency, in a subsequent study, researchers from the same group have prepared a 8 × 8 $PtSe_2$/Si heterojunction photodetector array.[187] Importantly, the $PtSe_2$/Si device manifests a short rise/decay time of 14.7/17.5 µs. Taking a step further, they use the planar device array to monitor the in-plane motion of a light spot and successfully achieve the monitoring of the "N" shape scanning trajectory (Fig. 7(f) and (g)), demonstrating the indisputable potency of 2DLM-based photodetectors in the field of micro-area target photoelectric tracking.

To date, the application and development of 2DLM based photodetectors in the field of photoelectric tracking of the micro-area target are still in the very initial stage. There are still a series of critical issues that need to be further addressed
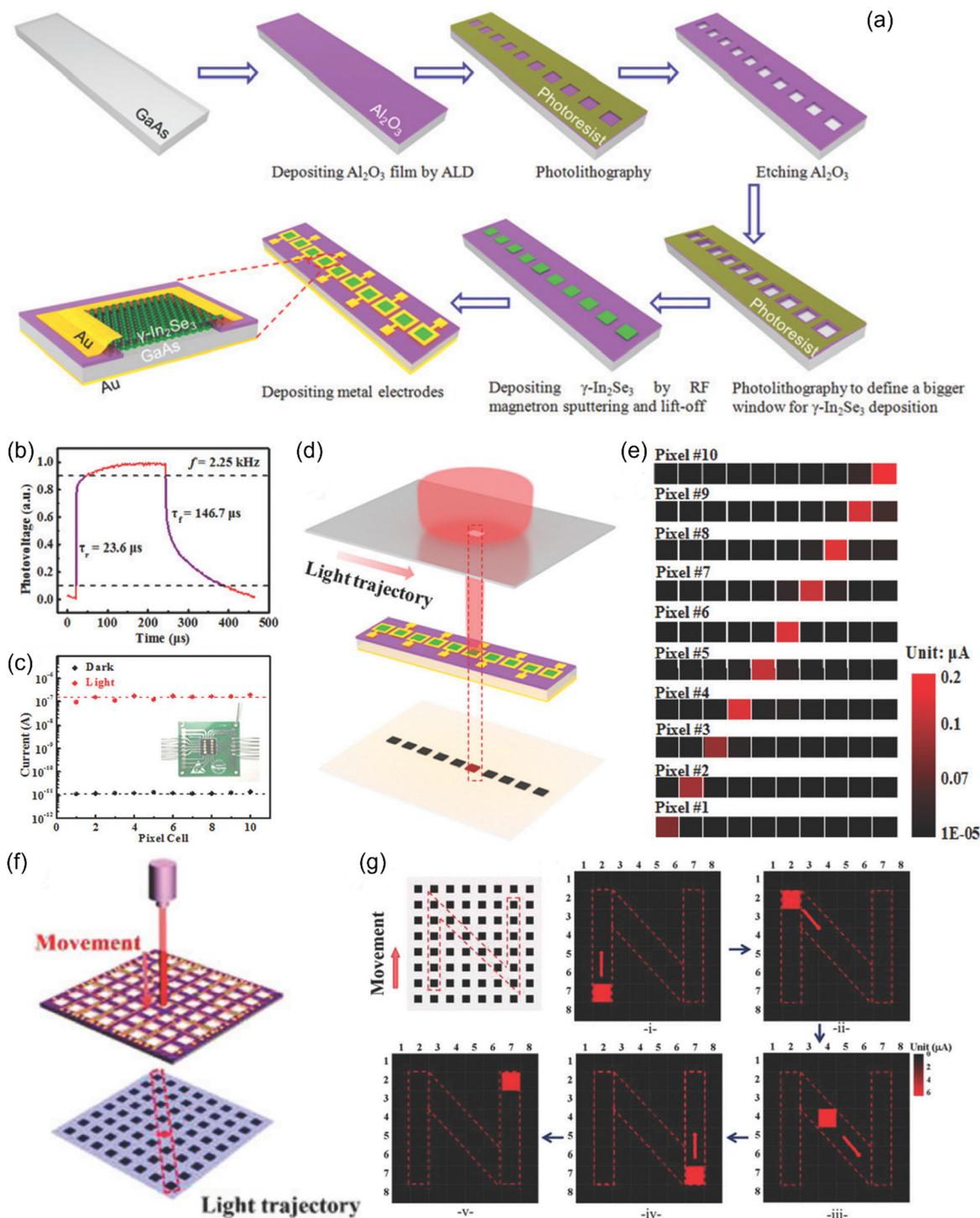
Fig. 7 (a) Schematic illustration of the fabrication process for constructing the linear γ-In$_2$Se$_3$/GaAs heterojunction photodetector array. (b) The temporal photoresponse of a γ-In$_2$Se$_3$/GaAs photodetector. (c) The channel current in the dark and under illumination of the γ-In$_2$Se$_3$/GaAs heterojunction photodetectors in the array. (d) Schematic diagram of the real-time light spot trajectory tracking. (e) Variation of the photocurrent of each pixel when the light spot moves through the array. Reproduced from ref. 186 with permission from the Royal Society of Chemistry, copyright 2020. (f) Schematic diagram of the real-time light spot trajectory tracking based on a planar PtSe$_2$/Si photodetector array. (g) Schematic diagram illustrating the light spot movement in an "N"-shaped trajectory and 2D current contrast maps showing the variation of the terminal current when the light spot moves through the array. Reproduced from ref. 187 with permission from Royal Society of Chemistry, copyright 2021.

prior to their practical commercialization. On one hand, the spatial resolution of the optoelectronic target tracking system still needs to be further improved to enable more precise location and motion trajectory monitoring. On the other hand,

as the preliminary exploration, the different device units in the above device arrays are electrically interconnected on account of the immature device design and manufacturing technology, which can result in undesirable crosstalk among different device units. To address the preceding issues, it is necessary to develop high-precision, non-destructive micro/nano processing technology for patterning 2DLMs and perform reasonable circuit design for signal readout in the upcoming future.

5. Optoelectronic logic operation

Optoelectronic logic devices combine photoelectric sensing and logic operations to achieve feature extraction and direct processing of incident optical information, significantly improving the efficiency of information identification and processing. These devices can markedly reduce the amount of data transmission and thus improve the response speed of the optoelectronic system. In addition, the development of optoelectronic logic devices will also promote the integration and innovation of optoelectronic technology, injecting new vitality into the domain of optoelectronics, which is of great significance for the progress of modern information technology. Profiting from the easy integration, excellent photosensitivity, and outstanding electrostatic controllability, 2DLM based photodetectors have shown considerable application prospects in the field of optoelectronic logic devices.

In 2022, Yang *et al.* prepared a Gr/h-BN/MoS$_2$ heterojunction photodetector with diverse photoresponse characteristics and achieved a series of reconfigurable non-volatile optoelectronic logic operations.[188] Fig. 8(a) shows the structure of the device, with MoS$_2$ as the transport channel and Gr as the floating gate. As shown in Fig. 8(b), the transport state of the device can be significantly adjusted by the gate voltage pulse. When a negative gate pulse is applied, the device turns to the low-resistance state (erase state), since electrons are pushed from graphene to MoS$_2$, leading to a positive float gate. When a positive gate pulse is applied, the device turns to a high-resistance state (program state), since electrons are driven from MoS$_2$ to graphene, leading to a negative float gate. As shown in Fig. 8(c), the device exhibits a bipolar photoresponse, depending on the initial conduction state. Starting from the program state, the photoresponse is positive, since the photogenerated holes are driven from MoS$_2$ to graphene. This will weaken the float-gate effect, and the channel current thus increases. In contrast, starting from the erase state, the photoresponse is negative, since the photogenerated electrons are driven from MoS$_2$ to graphene. This will also weaken the float-gate effect, and the channel current thus decreases. Subsequently, the device is used as the core functional component of Boolean logic operations. Logic inputs are the gate voltage and incident light, and the logic output is the source–drain current. By setting different initial states and inputting different signals at the input ends, "AND", "OR", "NAND", and "NOR" logic operations can be successfully achieved (Fig. 8(d)–(g)). Specifically, starting from the program state, neither small negative gate bias or weak light illumination can lead to a significant increase in the electrical conductance, whereas the simultaneous input can lead to a high output current, corresponding well to the "AND" logic function (Fig. 8(d)). Starting from the program state, either large negative gate bias or strong light illumination can lead to a significant increase in the electrical conductance, corresponding well to the "OR" logic function (Fig. 8(e)). Starting from the erase state, neither small positive gate bias or weak light illumination can lead to a significant decrease in the electrical conductance, whereas the simultaneous input can lead to low output current, corresponding well to the "NAND" logic function (Fig. 8(f)). Starting from the erase state, either large positive gate bias or strong light illumination can lead to a significant decrease in the electrical conductance, corresponding well to the "NOR" logic function (Fig. 8(g)). Overall, this study presents a flexible strategy for realizing multiple logic operations based on a single 2D vdWM photodetector with diverse photoresponse characteristics. Most recently, by using ultraviolet (UV) and blue illuminations as the input signals and using the SiC/graphene UV-visible dual-band photodetector as the sensing component, Zhang *et al.* have realized an "AND" optoelectronic logic gate, where the output signal is "1" only when both UV and visible illuminations are inputted.[189]

6. Ultraviolet monitoring

A radiation dosimeter is a kind of device that capitalizes on photoelectric conversion to monitor the surrounding radiation level. It is of great importance in a wealth of domains ranging from functional clothing, personal health, cosmetics, to medical treatment. Radiation dosimeter can remind people to prevent themselves from surrounding harmful radiation such as the fierce sunburn as well as X-ray in time, and thus help people avoid absorbing excessive radiation that can potentially damage their health. In the past decade, 2DLMs have demonstrated extensive advantages in radiation sensing, including high sensitivity, fast response rate, and ease of integration. In addition, the atomically thin nature of 2DLMs can endow the related optoelectronic devices with high transparency, excellent flexibility, and light weight, making them competitive in wearable devices. Accordingly, the photoelectric sensors made of 2DLMs are promising candidates for radiation monitoring.

Lee *et al.* developed a real-time, wireless, and wearable UVA monitoring patch based on porous reduced graphene oxide (pRGO) paper in 2022.[190] Compared to pristine graphene with a gapless band structure, the bandgap of reduced graphene oxide can be significantly opened,[191] which can prevent the photocarriers from recombining in an efficient way. In addition, the bandgap can be widely manipulated from 1.0 eV to 3.5 eV through tuning the reduction level,[192] providing a flexible approach to meet a targeted application. Impressively, the photocurrent of the pRGO paper photodetector largely remains invariable under both compressive and tensile bending treatments with a bending radius down to 2.0 mm (Fig. 9(a)). In
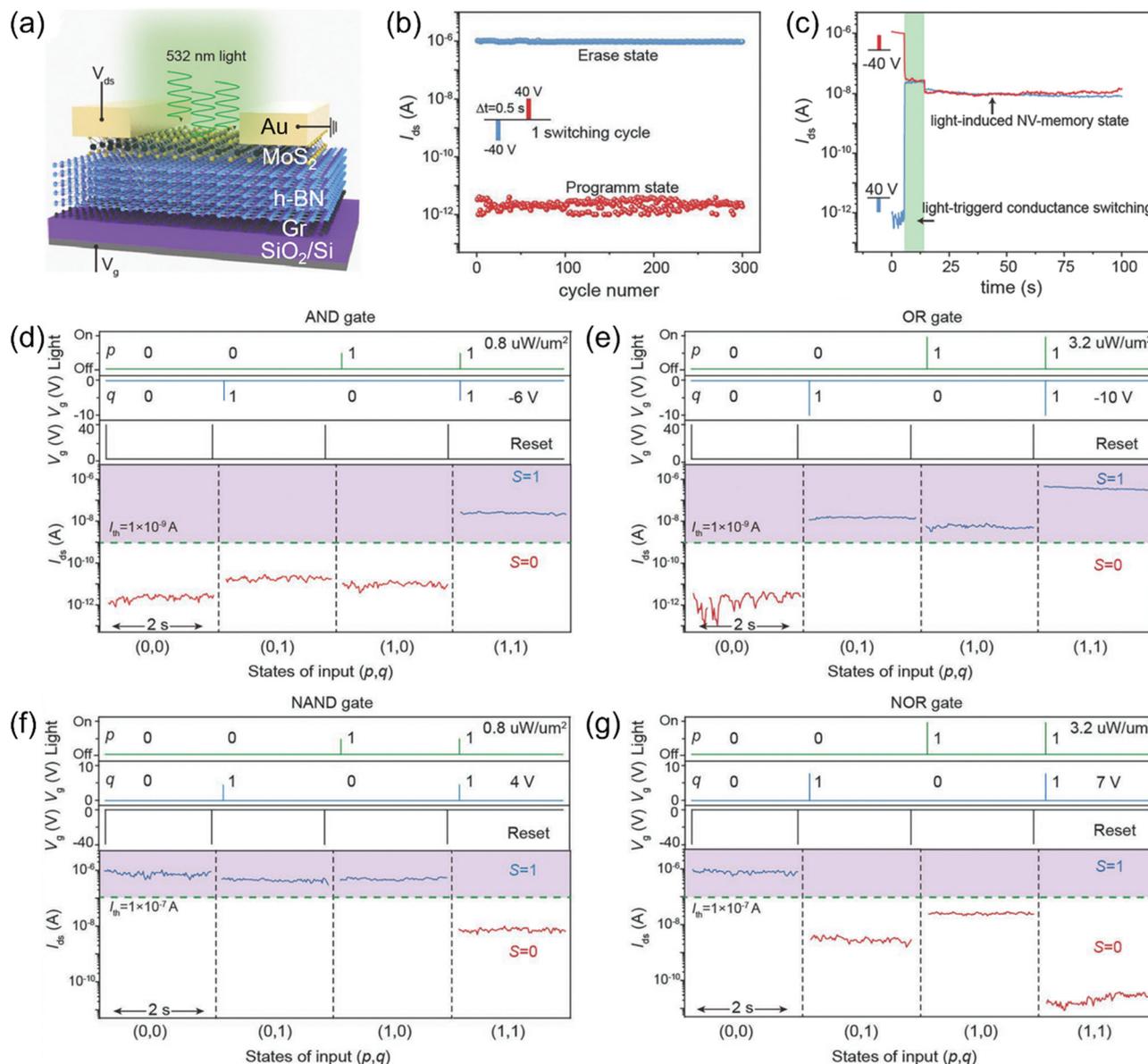
Fig. 8 (a) 3D schematic diagram of a Gr/h-BN/MoS$_2$ photodetector. (b) Program and erase states during multiple operation cycles. (c) Output current under various gate pulse and light pulse conditions. (d) AND, (e) OR, (f) NAND, and (g) NOR logic operations. Reproduced from ref. 188 with permission from John Wiley and Sons, Inc., copyright 2022.

addition, this pRGO device exhibits excellent anti-fatigue performance. Specifically, the photocurrent remains consistent even after 5000 bending cycles, as depicted in Fig. 9(b). As shown in Fig. 9(c), the distinct photoswitching characteristics has also been well maintained under bending operating conditions. This outstanding flexibility enables the pRGO devices to be flexibly integrated on various surfaces (Fig. 9(d)), without experiencing notable degradation in device properties, which substantially broadens the potential application scope in daily life. As such, the device has been further exploited for wearable real-time UVA monitoring. To achieve real-time and continuous ultraviolet radiation measurement, the device has been integrated with several components, including a flexible and bendable pRGO sensor, a microcontroller for real-time signal

processing, a bluetooth module for wireless signal transmission, a lithium polymer battery for power supply, and a graphical user interface (GUI) designed to display and alert about the UV radiation levels (Fig. 9(e)). To validate the function, two sets of experiments have been conducted, one performed outdoors and the other in a synthetic laboratory under controlled exposure to ultraviolet radiation with a wavelength of 365 nm and an intensity of 27.9 mW cm^{-2}. As shown in Fig. 9(f) and (g), real-time varying photocurrent reflecting the UVA level has been successfully recorded, verifying the outstanding UVA radiation monitoring capability of the pRGO patch.

As the expensive and complex manufacturing processes such as photolithography, high-temperature treatment and etching have been circumvented, the above wearable UVA
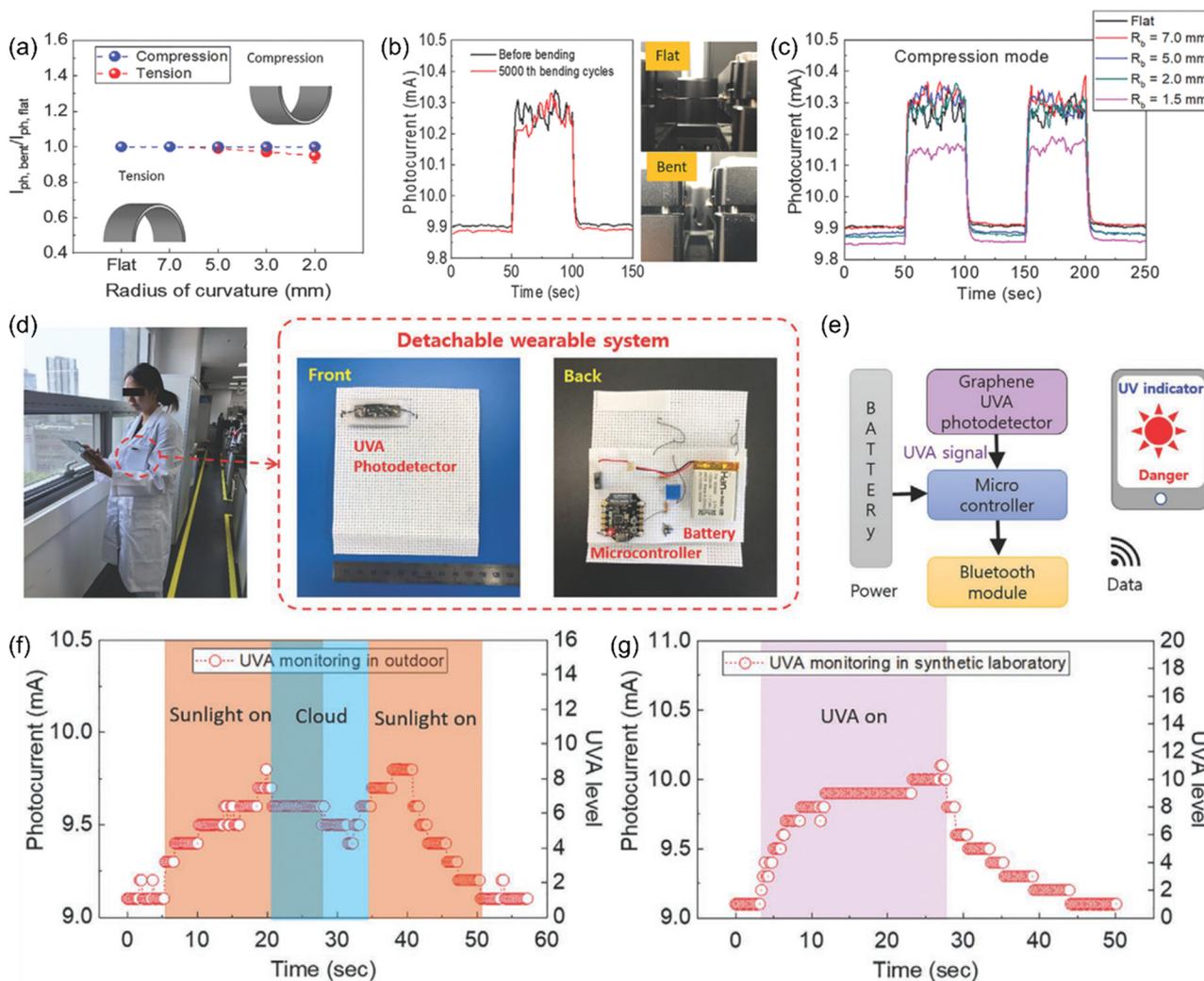
Fig. 9 Flexible pRGO photodetector and its application in a UVA dosimeter. (a) Normalized photocurrent as a function of the bending curvature radius upon compressive strain (blue dots) and tensive strain (red dots). (b) Photoswitching curves before bending (black line) and after 5000 bending cycles (red line). (c) Photoswitching curves upon bending treatments with various bending radii. (d) Photograph of a wireless pRGO UVA monitoring system attached onto a researcher (left). Photographs of the front view and the rear view of the detachable wearable system (right). (e) Functional block diagram of the wearable pRGO system. (f) Real-time UVA levels measured outdoor. The orange region and blue region represent sunny and cloudy conditions, respectively. (g) Real-time UVA levels measured in an indoor synthetic laboratory. The pink region represents UVA on. Reproduced from ref. 190 with permission from John Wiley and Sons, Inc., copyright 2022.

monitoring system is cost-effective. However, due to the presence of a lithium-polymer battery for the power supply, its volume and weight exceed those of many commercial portable systems. To solve this problem, Polat and collaborators have developed a UV skin exposure monitoring patch with a wireless power supply.[104] Specifically, the UV monitoring patch has integrated a flexible ultraviolet-sensitive GQD photodetector with a commercially available flexible near-field communication (NFC) circuit board, allowing wireless transmission of both power and data between the photodetectors and a smartphone. This design ensures battery-free operation for sensing the environmental UV index. In addition, a flexible short-pass light filter has been specifically designed to block the undesired light spectrum (>400 nm) and offers extra protection against mechanical strain.

Presently, the development and application of 2DLM-based photodetectors in UV radiation monitoring are still in the very initial stage. Several critical issues need further research attention. Firstly, the use of active devices will significantly increase the volume and reduce their integration capability. Although the wireless power transmission strategy has been developed, additional power consumption emerges as a derivative problem due to the low conversion efficiency. In recent years, van der Waals heterostructures such as MoS_2/WSe_2,[193] MoS_2/AsP,[194] and $WSe_2/graphene$[195] have been successfully developed as solar cells. In the upcoming future, these atomically thin solar cells can be used as the power sources for the radiation dosimeters to enable self-powered operation, which is conducive to further reducing the device's volume and weight. In addition, the previously reported devices have broadband

photoresponse. Therefore, in practical application, light filters are commonly needed to isolate surrounding visible and infrared light to prevent false alarm. This will increase the complexity of device design and preparation. Of note, large-bandgap materials have an inherent anti-interference ability for visible and near-infrared light. Fortunately, there have emerged a series of large-bandgap photosensitive 2DLMs, including NiPS$_3$,[196] GeSe$_2$,[197] α-MoO$_3$,[198] AsSbO$_3$,[199] GaPS$_4$,[200] and h-BN,[201] which are promising candidates for filter-free UV radiation dosimeters in the future.

7. Optical communication

Optical communication is a modern communication mode that uses light waves as the medium for information transmission.[202,203] The basic principle of optical communication is to convert the transmitted information into modulated optical signals, transmit them to the terminal through a medium such as optical fiber, and then convert the optical signals into electrical signals by the optical receiver, and finally restore them to the original information with the processor. Optical communication technology manifests a series of advantages, including low transmission loss, large transmission capacity, and strong resistance to electromagnetic interference, making it widely used in civil and military fields.

Currently, the light-sensing components of the modern optical communication systems are being confronted with a wealth of predicaments. Firstly, with the rapid development of modern information technology, the transmission distance of optical communications is constantly increasing, which inevitably leads to the attenuation of optical signals and the increase of noise level. Therefore, higher sensitivity and signal-to-noise ratio have always been anticipated to achieve reliable information transmission over longer distance. Secondly, modern information technology has been putting forward increasingly high demands for communication capacity, requiring a higher bandwidth, which demands a higher response rate for light-sensing devices. In addition, the optical communication systems are commonly subject to various forms of extrinsic interference, which may lead to a decrease in the signal quality and an increase of the transmission error rate. Accordingly, the light-sensing components need to possess a stronger anti-interference ability. Furthermore, in practical applications, the light-sensing components should also have characteristics such as low cost, environmentally friendly composition, and long lifetime to ensure large-scale, distributed, long-term, and stable optical communications, which are difficult to achieve with traditional materials. To address the afore-mentioned challenges, it is thus impending to explore new optoelectronic sensing candidate materials.

In this context, Lei and collaborators recently prepared high-performance Ta$_2$NiSe$_5$/GaN heterojunction photodetectors (Fig. 10(a)) and successfully exploited them for proof-of-concept optical information transmission.[204] Impressively, the on/off ratio of the device reaches $\approx 10^7$, which is of great significance for achieving a low error rate. The optimal responsivity and detectivity reach 1.22×10^4 A W^{-1} and 1.3×10^{16} Jones, respectively (Fig. 10(b)). Meanwhile, the response/recovery time is as short as 1.22/3.16 ms (Fig. 10(c)). Fig. 10(d) shows the typical experimental configuration of free space optical information transmission. In principle, the transmitted ASCII information is used to control the chopper, where "1" represents unblocked light and "0" represents blocked light. As a consequence, the generated light pulses will carry the required information for transmission. The light pulses are subsequently detected by the photodetector in the receiving end, generating two sets of states: high current state and low current state, representing "1" and "0" of the binary, respectively. After processing by the processor, the original information can be reproduced. As shown in Fig. 10(e), the Ta$_2$NiSe$_5$/GaN heterojunction photodetector has successfully achieved the accurate transmission of "LJP", verifying the important potential of 2DLM based photodetectors in the optical communication industry.

As for practical applications, optical fibers have been extensively used as the transmission mediums for optical communications because of their large communication capacity, low transmission loss, strong resistance to electromagnetic interference, excellent confidentiality, rich source materials, light weight, and good flexibility. In fiber optic communications, the loss of optical signals during transmission in optical fibers is an imperative element to consider. Generally, the most suitable wavelengths for fiber optic communications are 850 nm, 1310 nm, and 1550 nm, where the transmission loss is the lowest and the transmission distance is thus the longest.[207] However, the effective spectral window of many 2DLMs, such as the most commonly studied transition metal dichalcogenides (e.g., MoS$_2$, WS$_2$), cannot cover the most suitable wavelengths for the fiber optic communications mentioned above.[208] Therefore, it is urgent to explore new 2DLMs that can respond to the infrared bands and exploit them for optical information transmission applications. To this end, Zhang et al. prepared PdTe$_2$/WSe$_2$ heterojunction photodetectors and achieved optical information communication applications at 850 nm and 1310 nm (Fig. 10(f)).[205] Similarly, Zeng et al. prepared a graphene/PdTe$_2$/Si heterojunction photodetector and successfully achieved optical information transmission at 1550 nm (Fig. 10(g)).[206] Most recently, Xiong et al. constructed a β-In$_2$Se$_3$/Te broadband photodetector and harnessed it for optical communications at 1310 and 1550 nm.[209]

Although the above studies have achieved initial encouraging success, the high cost of the noble metal containing building blocks has severely hindered further large-scale practical applications. In recent years, a series of noble-element-free small-bandgap 2DLMs and their heterojunctions, such as black phosphorus,[210] In$_{1.75}$Sb$_{0.25}$Se$_3$,[211] Sb$_2$Te$_3$,[212] Bi$_2$Se$_3$,[213] Bi$_2$Te$_3$/Si,[214] WS$_2$/Bi$_2$Te$_3$,[215] WSe$_2$/Bi$_2$Te$_3$,[216] Bi$_2$O$_2$Se/Bi$_2$Se$_3$,[217] MoS$_2$/graphene/perovskite,[218] and WSe$_2$/Ta$_2$NiSe$_5$/WSe$_2$,[219] have been harnessed for infrared light sensing. These materials have enormous potential application value in the field of optical communications and they are worthy of further exploration in the upcoming future.
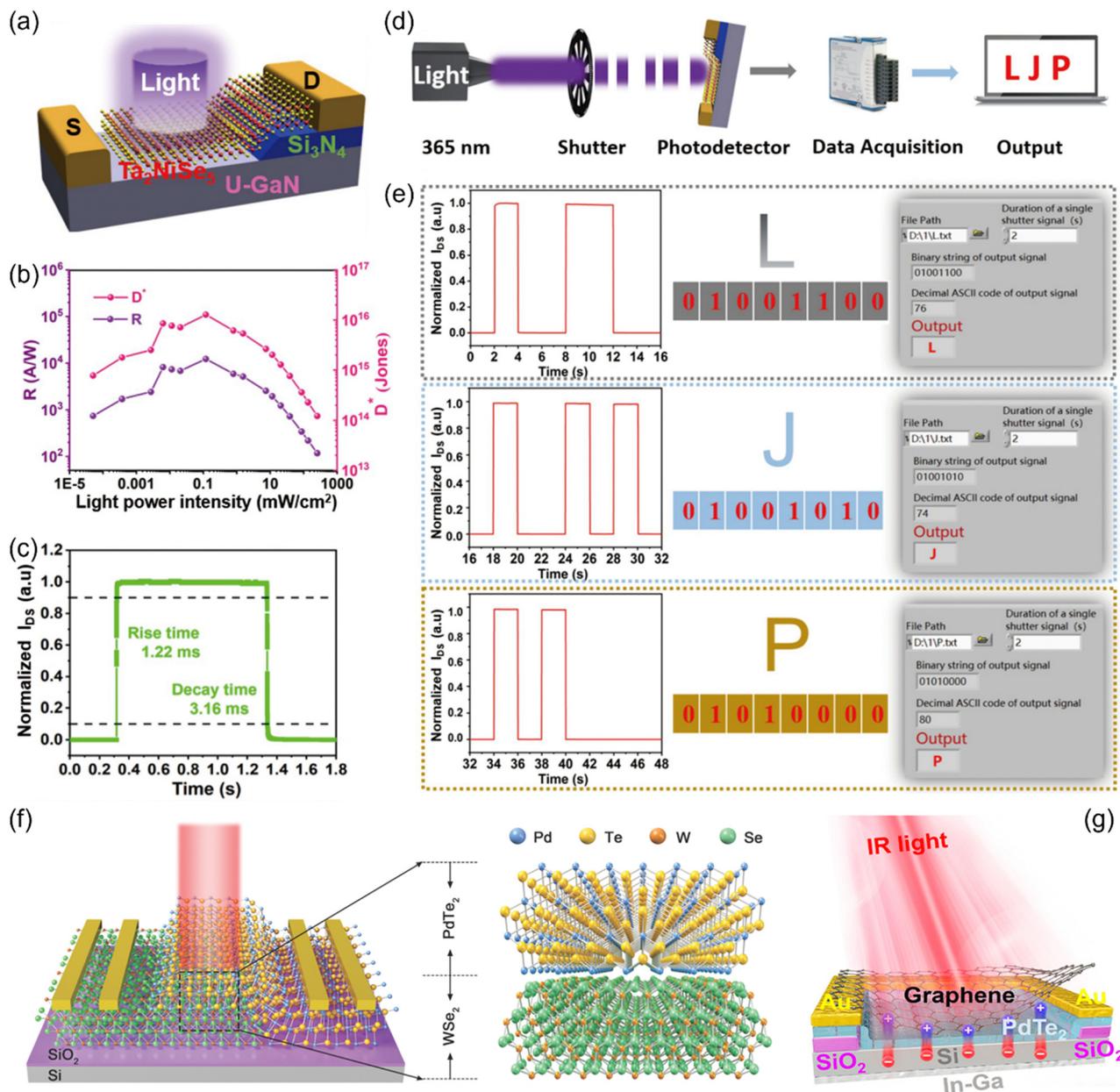
Fig. 10 (a) 3D schematic diagram of a Ta$_2$NiSe$_5$/GaN heterojunction photodetector. (b) Responsivity and detectivity as a function of light power intensity. (c) Response rate. (d) Schematic illustration of the experimental configuration for optical communications. (e) Proof-of-concept application demonstrating the successful transmission of the ASCII code of "LJP". Reproduced from ref. 204 with permission from Science China Press, copyright 2024. (f) 3D schematic diagram of a PdTe$_2$/WSe$_2$ heterojunction photodetector. Reproduced from ref. 205 with permission from John Wiley and Sons, Inc., copyright 2023. (g) 3D schematic diagram of a graphene/PdTe$_2$/Si heterojunction photodetector. Reproduced from ref. 206 with permission from American Chemical Society, copyright 2023.

To this end, in 2023, Ye *et al.* constructed a high-temperature-resistant photodetector (Fig. 11(a)) by using a large-bandgap AgInP$_2$S$_6$ nanosheet as the photosensitive channel and successfully harnessed it for high-temperature optical communication.[66] Research has found that AgInP$_2$S$_6$ photodetectors have excellent high-temperature resistance performance. Specifically, as the operating temperature increases from 24 °C to 160 °C, the device can maintain distinct optical switching characteristics (Fig. 11(b)). When the temperature returns to the initial temperature, the optical response of the device also roughly returns to the initial value. In addition, even when heated continuously at 150 °C for 10 hours, the device can still respond quickly and repetitively to periodically changing incident light (Fig. 11(c)). On this basis, the AgInP$_2$S$_6$ device was used as the optical signal receiving component to achieve the transmission of optical information at a working temperature of 160 °C. The obtained signal waveform is consistent with the results at room temperature (Fig. 11(d)).
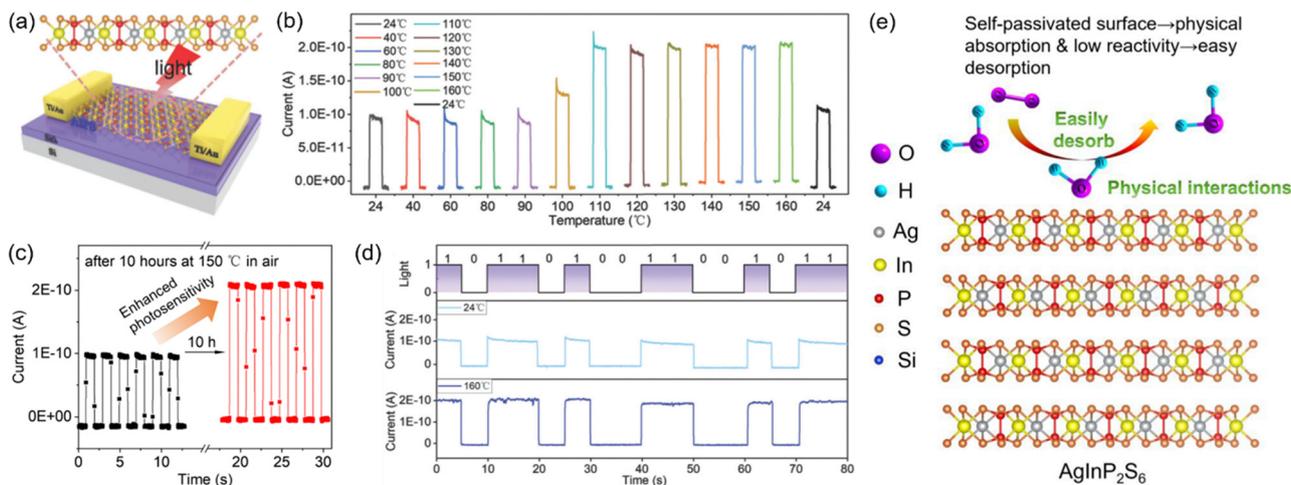
Fig. 11 (a) 3D schematic diagram of a AgInP$_2$S$_6$ photodetector. (b) Photoswitching curves under various working temperatures (24 to 160 °C). (c) Photoswitching curves of the AgInP$_2$S$_6$ photodetector before and after 10-hours of heating treatment in air at 150 °C. (d) Results of optical communications by using the AgInP$_2$S$_6$ photodetector as a light signal receiver under 24 and 160 °C. (e) Schematic illustration of the high stability of AgInP$_2$S$_6$ against the ambient species enabled by the self-passivated surface. Reproduced from ref. 66 with permission from John Wiley and Sons, Inc., copyright 2023.

The excellent immunity to high temperature of the AgInP$_2$S$_6$ devices is attributed to the synergy of multiple ingredients. Firstly, the bandgap of AgInP$_2$S$_6$ reaches $\approx$1.94 eV, which can significantly mitigate the intrinsic thermal excitation. Secondly, the covalent bonding between the atoms of AgInP$_2$S$_6$ is quite strong, which can suppress the decomposition caused by thermal disturbance. Finally, AgInP$_2$S$_6$ possesses a self-passivated surface, greatly suppressing its surface reactivity (Fig. 11(e)). On the whole, the above research has demonstrated that large-bandgap 2DLMs have enormous potential for application in high-temperature-proof optical communications. Thus far, researchers have discovered a series of large-bandgap 2DLMs, including InTeClO$_3$,[220] SnP$_2$S$_6$,[55] and GeSe$_2$.[221] In the future, the resistance to high temperature of these candidate materials and their application in high-temperature optical communications will be in need of further exploration.

In addition to power intensity, propagating light also carries other information such as polarization state and phase. The identification of these additional degrees can be exploited to further improve the efficiency of optical information transmission.[222,223] To this end, in 2022, Lu *et al.* prepared O–WS$_2$/WS$_2$ heterojunction photodetectors by using selective oxidation treatment, which was realized by e-beam lithography-assisted oxygen plasma irradiation.[105] With the advantage of the lowered geometric symmetry, the O–WS$_2$/WS$_2$ device exhibits a distinct polarization-dependent photoresponse, where the photoresponse reaches the maximum/minimum value upon illumination with perpendicular (90°)/parallel (0°) polarization. On this basis, proof-of-concept multiplexing optical communication application has been proposed and achieved by using this O–WS$_2$/WS$_2$ device as the optical signal receiving component (Fig. 12(a)). Specifically, the light intensity and polarization state are simultaneously used as independent

information transmission channels. Strong light represents "1" of the binary signal, and weak light represents "0". In addition, perpendicular polarization represents "1", and parallel polarization represents "0". Since the output signal of the O–WS$_2$/WS$_2$ photodetector depends on both light intensity and polarization state, there are a total of four levels of output photocurrent when the binary signals are transmitted through the two channels, which are denoted as level "4", level "3", level "2", and level "1" from high to low, corresponding to "strong light & perpendicular polarization", "strong light & parallel polarization", "weak light & perpendicular polarization", and "weak light & parallel polarization", respectively. In this study, the binary signal of "10101010" is used to program the light intensity, while a binary signal of "11011010" is used to program the polarization state (Fig. 12(b)). As shown in Fig. 12(c), the output photocurrent signal is "42324141", which can be decoupled into "1010101011011010" as per the preceding established relationship (Fig. 12(d)), successfully transmitting 16 signals in 8 readout cycles. Most recently, Pan *et al.* achieved the transmission of 32 binary signals in 16 readout cycles by taking use of the anisotropy-enabled quaternary outputs of a polarization-resolved ReSe$_2$/SnSe$_2$ photodetector.[170] On the whole, these studies provide new pathways for high-efficiency optical information transmission systems using 2DLM polarization-discriminating photodetectors as the light receiving components.

Apart from the information transmission efficiency, another imperative consideration for optical communications is the confidentiality of the transmitted data. Optical communications, serving as one of the most popular ways of modern information transmission, will deal with a substantially large amount of sensitive and confidential information. If transmitted without encryption, the information can be easily wiretapped, which may cause severe security risks. Encryption
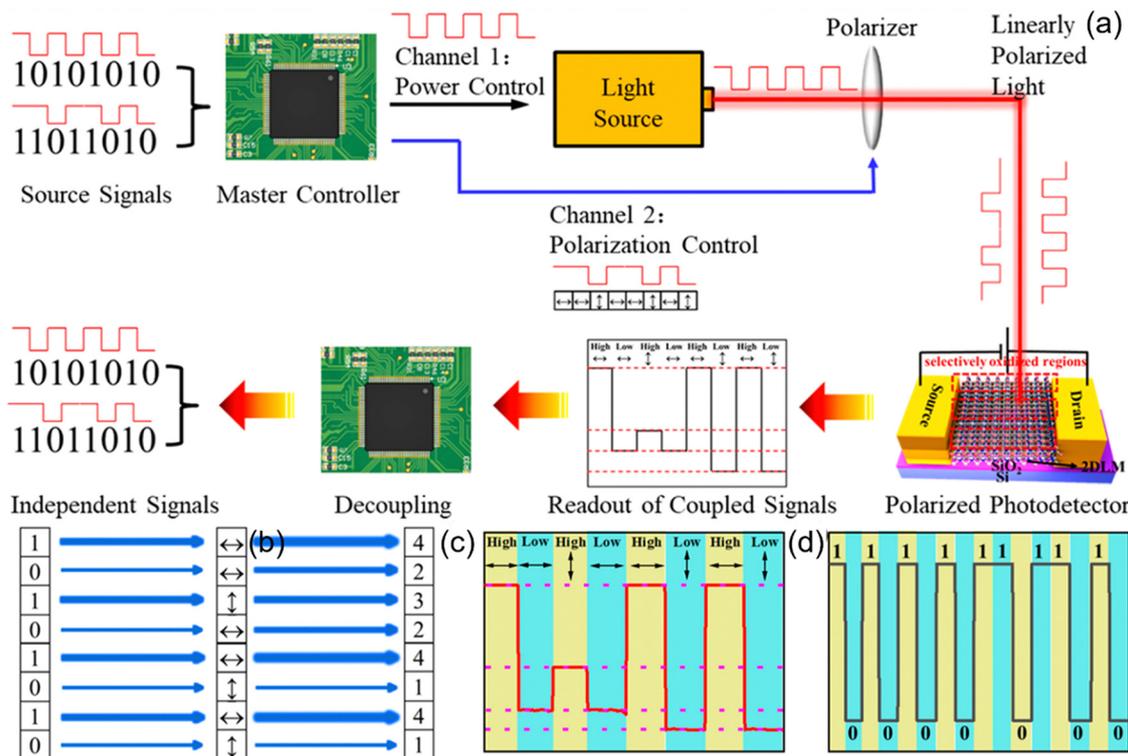
Fig. 12 (a) Schematic illustration of the mechanism for multiplexing optical communications. (b) Schematic illustration of the binary signals used for programming the light intensity and the polarization state. (c) The corresponding output current. (d) The decoupled binary signals according to the established relationship among output current, light intensity and polarization state. Reproduced from ref. 105 with permission from American Chemical Society, copyright 2022.

technology can effectively warrant data confidentiality, ensuring that the information will not be illegally accessed during transmission.[224] Therefore, encryption of optical communications plays an irreplaceable role in maintaining information security and ensuring communication reliability.

In 2023, Zhang et al. prepared a Gr/GaN heterojunction photodetector with a bipolar photoresponse (Fig. 13(a)) and demonstrated proof-of-concept encrypted optical communications by using this device as the light signal receiver.[225] Impressively, upon UV illumination, the device exhibits a negative photoresponse, whereas the photoresponse becomes positive upon red light illumination. The working mechanism of the bipolar photoresponse can be well explained using energy band diagrams. As shown in Fig. 13(b), under UV irradiation, a large number of photoexcited electron–hole pairs are generated in GaN. Under the drive of the interfacial built-in electric field, electrons flow into graphene (p-type), thereby increasing its Fermi level and reducing its conductivity (i.e., giving rise to negative photoresponse). As shown in Fig. 13(c), under red light irradiation, intrinsic excitation can hardly occur, but electrons from the valence band can be excited to the mid-gap states. As the number of trapped electrons increases, the interfacial potential barrier decreases, and holes thus inject into graphene, thereby lowering its Fermi level and leading to a positive photoresponse. Subsequently, the bipolar Gr/GaN photodetector is further applied to encrypted optical

communications. As shown in Fig. 13(d), the red light channel is used as the signal channel, while the ultraviolet light channel is used as the key channel. In the signal channel, interfering items will be inserted, which are labeled by the dark state of the key channel. As shown in Fig. 13(e), there are a total of four output modes depending on the two channels' inputs, namely "00", "01", "10", and "11", corresponding to "Red off & UV on", "Red on & UV on", "Red off & UV off", and "Red on & UV off". Fig. 13(f) presents the output result. According to Fig. 13(e) and (f), the input signals of the signal channel and the key channel are "110010" and "100111", respectively, resulting in an unencrypted signal of "1010" (Fig. 13(g)). On the whole, this study depicts a paradigm for the implementation of encrypted optical communications based on 2DLM photodetectors with a bipolar photoresponse.

Another pivotal factor determining the potential for application in optical communications is the response rate. Thus far, the response time of the majority of 2DLM based photodetectors has still been relatively long, mostly in the millisecond to microsecond range, which is disadvantageous to the data transmission efficiency. Fortunately, device structure optimization has proven to be an effective strategy for improving response rate. For example, by constructing vertical Gr/WSe$_2$/Gr photodetectors, Massicotte et al. achieved a response time as short as 5.5 ps.[226] In another research work, by using graphene as the bottom electrode to enable vertical carrier transport,
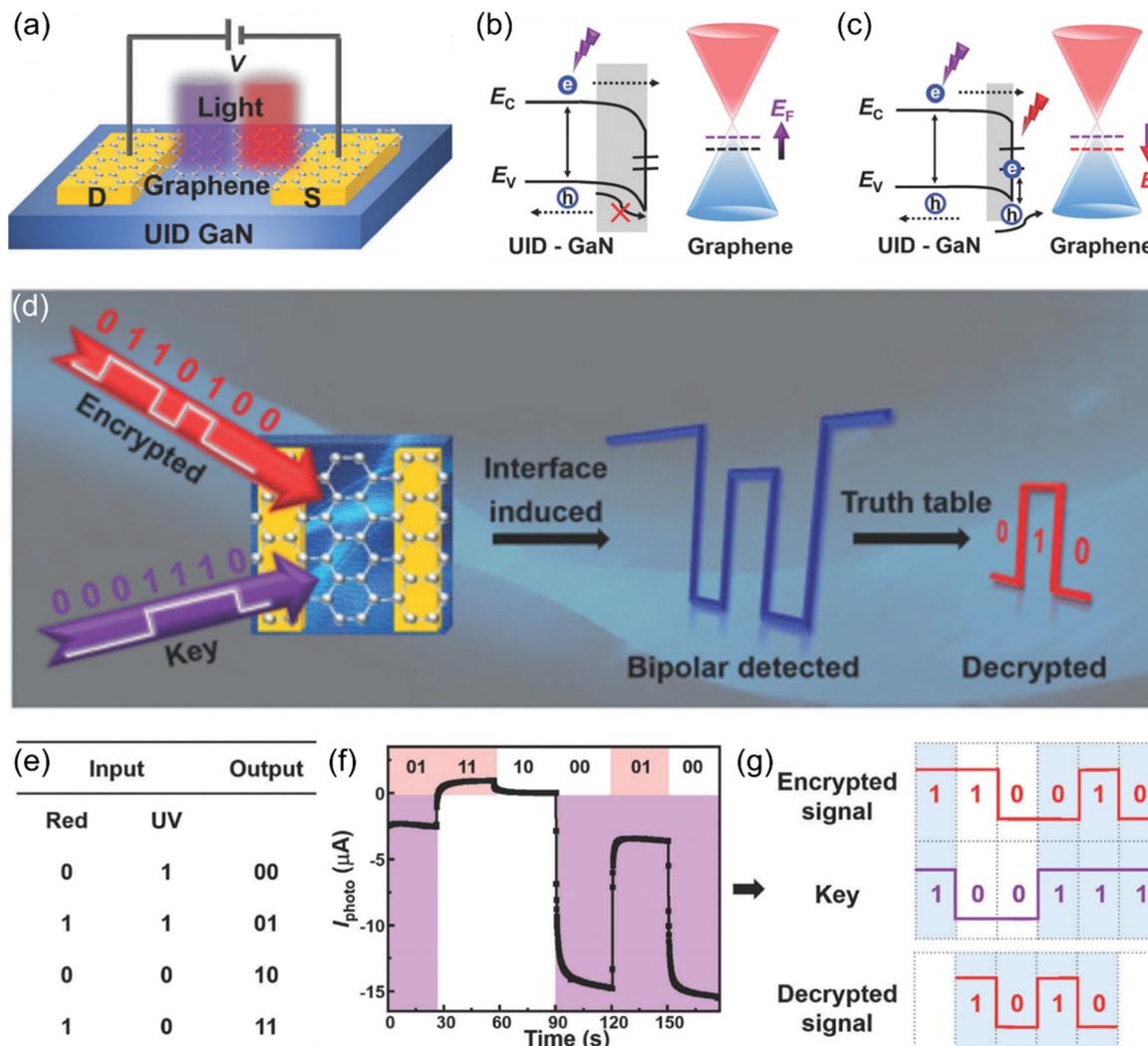
Fig. 13 (a) 3D schematic diagram of the Gr/GaN photodetector. (b) and (c) Energy band diagrams of the Gr/GaN photodetector upon UV and red light illuminations, respectively. (d) Schematic illustration of the encrypted optical communications by using the bipolar Gr/GaN photodetector as the light receiver. (e) The one-to-one logical relationship between photocurrent levels and states of incident light. (f) The output photocurrent. (g) The decoupled channel signal, the key, as well as the decoded signal. Reproduced from ref. 225 with permission from John Wiley and Sons, Inc., copyright 2023.

Dai *et al.* increased the response rate of the Au/InSe Schottky junction photodetector by approximate three orders of magnitude.[227] In the future, more device optimization schemes should be designed to accelerate the transport and collection of photocarriers, finally shortening the response time of various 2DLM based photodetectors.

8. Automatic driving

Automatic driving is an emerging intelligent technology that capitalizes on advanced sensing systems and image processing algorithms to achieve unmanned operation. Lidar is one of the core components of automatic driving technology, which is a device that uses laser beams to identify targets. Basically, when an emitted laser beam is irradiated on a target, some of the light will be reflected. The light receiver detects the reflected light signal and restores it to an electrical signal. Through

signal processing, various information about the target, including distance, motion direction, speed, shape, *etc.*, can be obtained. In this consideration, photodetectors are the core components of LiDAR, serving as the "eyes". Currently, the light-sensing components of LiDAR has been facing a series of tricky challenges, including large volume, low sensitivity, and high cost. Therefore, it is urgent to explore new potential materials. 2DLMs have the advantages of thin thickness, light weight, and strong interaction with light, thus manifesting important application potential in LiDAR next-generation technology.

As a pioneering attempt, in 2023, Luo *et al.* prepared a high-performance $WSe_2/WS_2/WSe_2$ dual-junction phototransistor (Fig. 14(a)) and successfully implemented an automatic driving function by exploiting it as the light signal receiver.[228] The optimal responsivity and detectivity of the device reached 35.4 A W^{-1} and 1.9×10^{14} Jones, respectively (Fig. 14(b)). In addition, the response/recovery time of the device is as short as
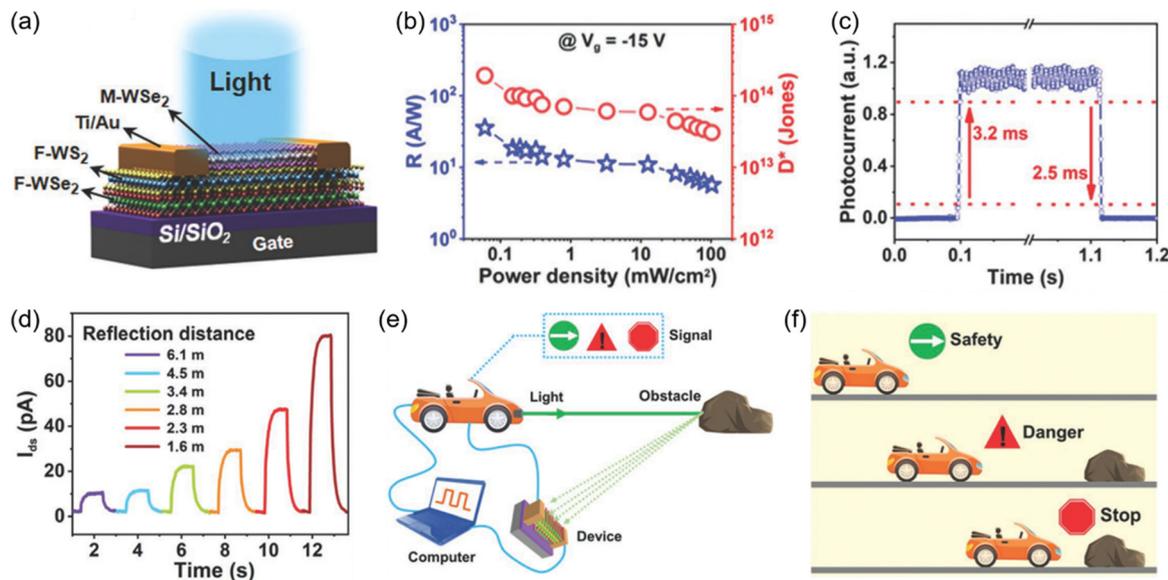
Fig. 14 (a) 3D schematic diagram of a WSe$_2$/WS$_2$/WSe$_2$ dual-junction photodetector. (b) Responsivity and detectivity as a function of light power density. (c) Temporal photoresponse. (d) Photoswitching curves upon illumination with various reflectance distances. (e) and (f) Schematic illustration on the working principle of the automatic driving system by using the WSe$_2$/WS$_2$/WSe$_2$ photodetector as the light signal receiver. Reproduced from ref. 228 with permission from John Wiley and Sons, Inc., copyright 2022.

3.2/2.5 ms (Fig. 14(c)). Further investigation has determined that the device can accurately identify light signals reflected back from different distances. As shown in Fig. 14(d), as the reflection distance decreases, the photoresponse gradually increases, laying a solid foundation for recognizing the distance of the target. Finally, the WSe$_2$/WS$_2$/WSe$_2$ photodetector is used as an optical signal receiver for LiDAR and successfully implements the proof-of-concept automatic braking function (Fig. 14(e) and (f)). In a subsequent research work, the same research group has used an In$_2$Se$_3$/h-BN/CsPb(Br/I)$_3$ heterostructure photodetector as the optical signal sensing component to achieve the proof-of-concept automatic obstacle avoidance function.[229] The preceding studies have fully portended the enormous potential of 2DLM based photodetectors in automatic driving applications.

Nevertheless, the above-mentioned studies have mainly focused on the visible band. In practical applications, infrared lights (*e.g.*, 905 nm,[230] 1550 nm[231]) are much more favorable. On one hand, infrared light will not interfere with human vision. Meanwhile, it causes little radiation damage to the human eye. On the other hand, it has an excellent anti-interference ability and can accurately capture and measure targeted objects in complex environments (*e.g.*, foggy day, hazy day). In the future, more research efforts should be focused on intelligent driving technology using 2DLM based infrared photodetectors as the optical signal sensing units.

9. Acoustic signal detection

Voiceprint detection is a technique that utilizes individual features contained in voice signals for identity recognition.

The acoustic characteristics of each individual are unique, because there are slight differences in their vocal organs and language habits, which can lead to changes in the airflow of their voice, thereby resulting in differences in sound quality and timbre. Voiceprint detection has potential application value in a variety of critical fields, such as information security and non-contact control, which can improve security and efficiency, and promote the development of social informatization and intelligence. Recently, the perception of acoustic vibrations through light sensing has been demonstrated, especially using invisible light to augment detection confidentiality. This approach has significant advantages. For example, it offers a unique opportunity for amalgamating the detection process of visual and auditory stimuli. Compared with other commonly used devices, such as capacitive sensors and piezoelectric sensors, photodetectors prepared with 2DLMs have a higher response speed.

Most recently, Fu *et al.* designed a vertically stacked graphene/Ge (Gr/Ge) hybrid field-effect phototransistor and harnessed it for the acquisition and modulation of auditory signals.[232] By controlling the gate voltage, the interplay of source–drain current (I_{ds}) and gate leakage current (I_g) in this device results in continuously tunable positive photocurrent (PPC) and negative photocurrent (NPC). As shown in Fig. 15(a), when the gate voltage falls below the threshold voltage, the Gr/Ge heterojunction appears to be forward-biased. In this case, the graphene channel and the Gr/Ge junction can be regarded as two resistors. When the device is illuminated, photocarriers are generated, reducing their resistance. Since the directions of I_{ds} and I_g are consistent, the two flows will cooperate with each other to generate PPC. In contrast, when $V_{bg} > V_{th}$, the Gr/Ge junction is reverse-biased. Under illumination, the graphene's
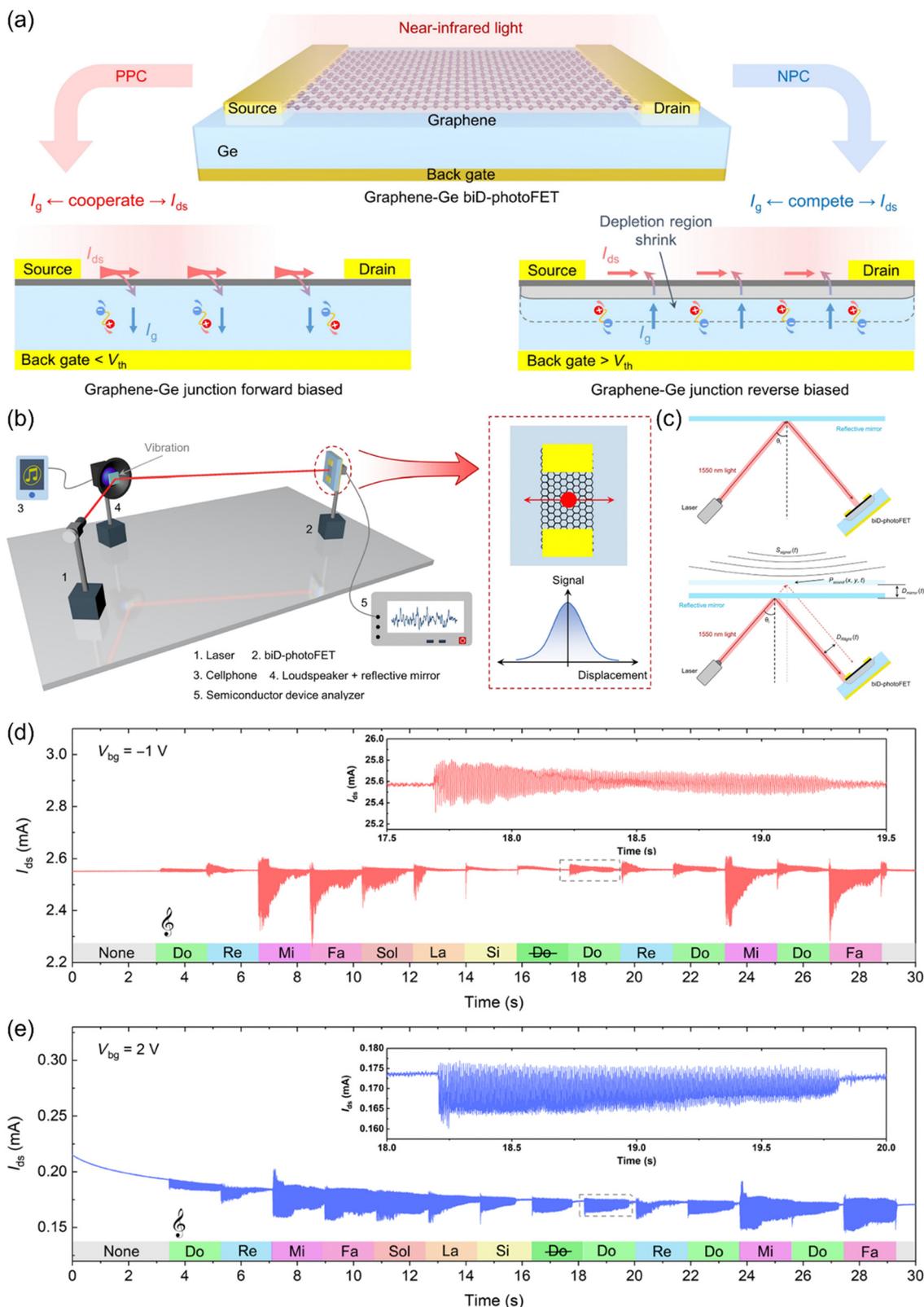
Fig. 15 (a) Schematic illustration of the device structure of a Gr/Ge hybrid field-effect phototransistor and its working mechanism. (b) Schematic illustration of the measurement configuration for acoustic signal detection. (c) Schematic illustration of the effect of the acoustic wave on the optical signal reaching the device. (d) and (e) Output current without no acoustic input and with various acoustic inputs under the back gate voltage of −1 V and 2 V. Reproduced from ref. 232 with permission from American Chemical Society, copyright 2024.

resistance is reduced and the heterojunction depletion layer is shrunk. Therefore, the Gr/Ge junction becomes a low-resistance resistor, and I_{ds} and I_g are opposite. As a result, the two flows will compete with each other to produce NPC. Following the realization of the tunable photoresponse, the Gr/Ge hybrid field-effect phototransistor is used to detect auditory signal by leveraging the high responsivity and fast response speed. The experimental configuration is schematically shown in Fig. 15(b). A 1550 nm laser beam is directed onto a reflector in front of the sound source, after which it is reflected and detected by the Gr/Ge field-effect phototransistor. In principle, the acquisition and recording of the voice signal are realized by adjusting the laser's path. When the acoustic pressure interacts with the reflective mirror, it will make it move. The reflected light's position and the energy reaching the active area of the photodetector change accordingly (Fig. 15(c)). Consequently, the output photocurrent changes, recording the "shape" of the corresponding sound waves. Fig. 15(d) and (e) present the note signals captured by the Gr/Ge field-effect phototransistor at different gate voltages. Apparently, different notes generate different shapes of the I–t signals, laying a solid foundation for voiceprint detection. More importantly, the signal intensity recorded at a gate voltage of –1 V is higher than that recorded at +2 V, demonstrating the capacity of gate voltage modulation to amplify or attenuate sound waves, resembling the regulation mechanism of the human auditory system. On the whole, this study depicts an attractive paradigm for realizing voiceprint detection based on 2DLM photodetectors.

10. Conclusion & perspective

In summary, benefiting from the unique properties spanning excellent flexibility, pronounced electrostatic tunability, diversified electronic band structures, dangling-bond-free surface, and ease of integration, a wealth of research advancements have been accomplished in the field of optoelectronic applications by leveraging 2DLM photodetectors. To date, these devices have been widely applied in a variety of fields such as imaging, health monitoring, target tracking, optoelectronic logic operation, ultraviolet monitoring, optical communications, automatic driving, and acoustic signal detection, revealing enormous potential towards the next generation of photodetection. However, in the current stage, there are still some critical issues to be addressed, which have been epitomized below, along with the potential solutions addressing them.

(A) One important ingredient restricting the further development of optoelectronic applications based on 2DLMs is their relatively poor photosensitivity. On account of the atomically thin thickness of 2DLMs, their light absorption is rather low, and their carrier lifetime is quite short. These together lead to the overall low photosensitivity of 2DLM photodetectors. Therefore, in the future, two approaches can be exploited to further improve the photosensitivity of 2DLM photodetectors. On the one hand, 2DLM photodetectors can be coupled with a plasmonic optical antennas/resonant metasurface to achieve localization of light through plasmonic resonance, thereby enhancing the interactions between 2DLMs and light.[208,233] On the other hand, built-in electric fields or type II band arrangements can be introduced through band engineering and construction of heterostructures to extend the lifetime of photocarriers.[234–236]

(B) Another pivotal ingredient standing in the way of further development lies in the difficulty of scalable preparation of high-quality 2DLMs. Thus far, many exploratory studies on downstream optoelectronic applications have been conducted based on mechanical exfoliation technology.[66,105,137] However, mechanical exfoliation technology usually only produces 2D nanosheets with a lateral scale of tens of micrometers, and its production yield is extremely low, and is far from meeting the needs of practical production and commercialization. Accordingly, there is an urgent demand to search for alternative preparation approaches. In view of this, MOCVD,[237] MBE,[238] CVD,[239] and PLD[153] can be potential approaches to overcoming this challenge.

(C) Although a variety of downstream applications have been realized using 2DLM photodetectors, the optoelectronics industry is an enormous industry. There are still extensive fields to be explored, such as wearable X-ray radiometers, bionic navigation, guidance, space exploration, *etc.*

As a concluding remark, photodetectors built of 2DLMs have demonstrated indisputable potential in a variety of optoelectronic devices. Although the prototype photodetectors have been widely explored, the investigation on the upcoming downstream applications is still in the early stage. There are still critical issues to be addressed. Looking ahead, by overcoming the existing challenges, it is envisioned that 2DLM photodetectors will play an imperative role in promoting the next-generation optoelectronic industry.

Data availability

No primary research results, software or code have been included and no new data were generated or analysed as part of this review.

Conflicts of interest

The authors declare no competing interests.

Acknowledgements

References

1 Z. Li, T. Yan and X. Fang, *Nat. Rev. Mater.*, 2023, **8**, 587–603.

2 Z. Zheng, J. Yao, J. Li and G. Yang, *Mater. Horiz.*, 2020, **7**, 2185–2207.

3 H. Lu, W. Wu, Z. He, X. Han and C. Pan, *Nanoscale Horiz.*, 2023, **8**, 1014–1033.

4 T. Araki, K. Li, D. Suzuki, T. Abe, R. Kawabata, T. Uemura, S. Izumi, S. Tsuruta, N. Terasaki, Y. Kawano and T. Sekitani, *Adv. Mater.*, 2023, **36**, 2304048.

5 L. Li and G. Shen, *Mater. Horiz.*, 2023, **10**, 5457–5473.

6 N. Zhang, X. Gao, H. Guan, S. Sun, J. Liu, Z. Shao, Q. Gao, Y. Zhang, R. Sun, G. Yang, F. Gao and W. Feng, *Nano Res.*, 2024, **17**, 4471–4477.

7 M. Kumar and H. Seo, *Adv. Opt. Mater.*, 2023, **11**, 2301165.

8 M. Deng, Z. Li, X. Deng, Y. Hu and X. Fang, *J. Mater. Sci. Technol.*, 2023, **164**, 150–159.

9 Y. Wang, L. Peng, J. Schreier, Y. Bi, A. Black, A. Malla, S. Goossens and G. Konstantatos, *Nat. Photonics*, 2024, **18**, 236–242.

10 X. Cai, H. Zhang, P. Wei, Q. Liu, D. Sheng, Z. Li, B. Zhang, G. Tang, W. Zhao, Z. Ye, Z. Xue, Y. Xie, Y. Dai, C. Wang, Y. Wang, X. Fu, L. Yin, H. Peng, H. Ding, G. Zhao and X. Sheng, *Nat. Photonics*, 2024, **18**, 492–500.

11 P. Wang, W. Xue, W. Ci, R. Yang and X. Xu, *Mater. Futures*, 2023, **2**, 035301.

12 J. Qi, Z. Wu, W. Wang, K. Bao, L. Wang, J. Wu, C. Ke, Y. Xu and Q. He, *Int. J. Extreme Manuf.*, 2023, **5**, 022007.

13 K. Cho, T. Lee and S. Chung, *Nanoscale Horiz.*, 2022, **7**, 1161–1176.

14 X. Hang, X. Shengjie, X. Xun, Z. Jincheng, H. Weichang and D. Yi, *Microstructures*, 2022, **2**, 2022011.

15 H. Xue, W. Gao, J. Gao, G. F. Schneider, C. Wang and W. Fu, *Int. J. Extreme Manuf.*, 2023, **5**, 032010.

16 A. Mondal and M. De, *Tungsten*, 2024, **6**, 1–16.

17 J. Han, F. Wang, Y. Zhang, W. Deng, M. Dai, F. Hu, W. Chen, J. Cui, C. Zhang, S. Zhu, C. Wang, M. Ye, S. Han, Y. Luo, T. Zhai, J. Wang and Q. J. Wang, *Adv. Mater.*, 2023, **35**, 2305594.

18 Q. Ye, J. Lu, H. Yi, Z. Zheng, C. Ma, C. Du, Y. Zou, J. Yao and G. Yang, *Appl. Phys. Lett.*, 2022, **120**, 181104.

19 P. Chen, L. Pi, Z. Li, H. Wang, X. Xu, D. Li, X. Zhou and T. Zhai, *Appl. Phys. Lett*, 2022, **121**, 021103.

20 H. Zhang, Z. Wang, J. Chen, C. Tan, S. Yin, H. Zhang, S. Wang, Q. Qin and L. Li, *Nanoscale*, 2022, **14**, 16130–16138.

21 S. Yang, P. Luo, F. Wang, T. Liu, Y. Zhao, Y. Ma, H. Li and T. Zhai, *Small*, 2022, **18**, 2105211.

22 S. Wang, Y. Bai, M. Liu, X. Zong, W. Wang, Q. Mu, T. Han, F. Li, S. Wang, L. Shan and M. Long, *Nanoscale*, 2023, **15**, 17006–17013.

23 Q. Zhang, B. Zhao, S. Hu, R. Tian, C. Li, L. Fang, Y. Zhang, Y. Liu, J. Zhao and X. Gan, *Nanoscale*, 2023, **15**, 15761–15767.

24 H. Mu, R. Zhuang, N. Cui, S. Cai, W. Yu, J. Yuan, J. Zhang, H. Liu, L. Mei, X. He, Z. Mei, G. Zhang, Q. Bao and S. Lin, *ACS Nano*, 2023, **17**, 21317–21327.

25 X. Cao, S. Yan, Z. Li, Z. Fang, L. Wang, X. Liu, Z. Chen, H. Lei and X. Zhang, *J. Phys. Chem. Lett.*, 2023, **14**, 11529–11535.

26 D. P. Do, C. Hong, V. Q. Bui, T. H. Pham, S. Seo, V. D. Do, T. L. Phan, K. M. Tran, S. Haldar, B. Ahn, S. C. Lim, W. J. Yu, S. G. Kim, J. H. Kim and H. Lee, *Adv. Sci.*, 2023, **10**, 2300925.

27 H. Yi, H. Yang, C. Ma, Y. Ma, Q. Ye, J. Lu, W. Wang, Z. Zheng, Z. Deng, Y. Zou, J. Yao and G. Yang, *Sci. China Mater.*, 2023, **66**, 1879–1890.

28 Y. Wang, W. Zhai, Y. Ren, Q. Zhang, Y. Yao, S. Li, Q. Yang, X. Zhou, Z. Li, B. Chi, J. Liang, Z. He, L. Gu and H. Zhang, *Adv. Mater.*, 2023, **36**, 2307269.

29 H. Wang, Y. Li, P. Gao, J. Wang, X. Meng, Y. Hu, J. Yang, Z. Huang, W. Gao, Z. Zheng, Z. Wei, J. Li and N. Huo, *Adv. Mater.*, 2023, **36**, 2309371.

30 S. Li, J. Zhang, L. Zhu, K. Zhang, W. Gao, J. Li and N. Huo, *Adv. Funct. Mater.*, 2023, **33**, 2210268.

31 M. Jiang, T. Zheng, J. Zhang, Z. Li, Q. Deng, Y. Pan, W. Gao, Y. Yang, J. Li and N. Huo, *Adv. Opt. Mater.*, 2024, **12**, 2303217.

32 S. Xiao, T. Zheng, W. Chen, J. Zhang, M. Yang, Y. Sun, Z. Zheng, D. Hao, N. Huo, Z. Chen and W. Gao, *Adv. Funct. Mater.*, 2024, 2403509.

33 M. R. Lien, N. Wang, J. Wu, A. Soibel, S. D. Gunapala, H. Wang and M. L. Povinelli, *Nano Lett.*, 2022, **22**, 8704–8710.

34 S. M. Koepfli, M. Baumann, Y. Koyaz, R. Gadola, A. Güngör, K. Keller, Y. Horst, S. Nashashibi, R. Schwanninger, M. Doderer, E. Passerini, Y. Fedoryshyn and J. Leuthold, *Science*, 2023, **380**, 1169–1174.

35 J. Xue, S. Wang, J. Zhou, Q. Li, Z. Zhou, Q. Hui, Y. Hu, Z. Zhou, Z. Feng, Q. Yan, Y. Yu, Y. Weng, R. Tang, X. Su, Y. Xin, F. Zheng, S. Ju, L. You and L. Fang, *Appl. Phys. Lett*, 2023, **122**, 181903.

36 M. Huang, M. Wang, C. Chen, Z. Ma, X. Li, J. Han and Y. Wu, *Adv. Mater.*, 2016, **28**, 3481–3485.

37 M. Yang, W. Gao, Q. Song, Y. Zhou, L. Huang, Z. Zheng, Y. Zhao, J. Yao and J. Li, *Adv. Opt. Mater.*, 2021, **9**, 2100450.

38 X. Guo, Y. Wang, A. Elbourne, A. Mazumder, C. K. Nguyen, V. Krishnamurthi, J. Yu, P. C. Sherrell, T. Daeneke, S. Walia, Y. Li and A. Zavabeti, *Nanoscale*, 2022, **14**, 6802–6810.

39 H. Jang, Y. Song, Y. Seok, H. Im, T. H. Kim, J. H. Lee, Y. H. Kim and K. Lee, *Nanoscale*, 2022, **14**, 3004–3012.

40 C. C. S. Maria, P. H. Wu, D. P. Hasibuan, C. S. Saragih, H. Giap, D. H. Nguyen, Y. R. Chen, R. A. Patil, D. V. Pham, J. L. Shen, C. C. Lai, M. K. Wu and Y. R. Ma, *J. Mater. Chem. C*, 2023, **11**, 14316–14325.

41 J. Chen, S. Lu, Y. Hu, F. Yang, H. Han, L. Kong, B. He, S. Ruan and B. Xiang, *Adv. Opt. Mater.*, 2024, **12**, 2301543.

42 X. Li, X. Chen, S. Li, F. Chu, W. Deng, X. Zhang, J. Li, X. Bao, B. An, C. You, F. Liu and Y. Zhang, *Nanoscale*, 2021, **13**, 16448–16456.

43 Y. Yang, J. Li, S. Choi, S. Jeon, J. H. Cho, B. H. Lee and S. Lee, *Appl. Phys. Lett*, 2021, **118**, 013103.

44 M. Yang, Z. Luo, W. Gao, M. Zhang, L. Huang, Y. Zhao, J. Yao, F. Wu, J. Li and Z. Zheng, *Adv. Opt. Mater.*, 2022, **10**, 2200717.

45 Z. Muhammad, F. Wali, G. Hussain, R. Islam, S. Ullah, P. Wu, F. Khan, C. Autieri, Y. Zhang, T. Alshahrani and W. Zhao, *J. Mater. Chem. C*, 2023, **11**, 2608–2618.

46 M. Jiang, X. Pan, K. Zhang, S. Tian, L. Zhang, L. Han, Y. He, X. Lv, S. Lan, H. Xing and L. Wang, *Adv. Electron. Mater.*, 2024, **10**, 2300742.

47 Z. Zhao, F. Dong, Y. Wang, J. Sun, H. Ye, R. Wang and J. Zhang, *Nanoscale*, 2023, **15**, 11955–11962.

48 Y. Yu, M. Peng, F. Zhong, Z. Wang, X. Ge, H. Chen, J. Guo, Y. Wang, Y. Chen, T. Xu, T. Zhao, T. He, K. Zhang, F. Wu, C. Chen, J. Dai and W. Hu, *Mater. Horiz.*, 2023, **10**, 2579–2586.

49 Y. Tian, Y. Cheng, J. Huang, S. Zhang, H. Dong, G. Wang, J. Chen, J. Wu, Z. Yin and X. Zhang, *Nano Res.*, 2022, **15**, 6628–6635.

50 S. Zhang, Y. Hao, F. Gao, X. Wu, S. Hao, M. Qiu, X. Zheng, Y. Wei and G. Hao, *2D Mater.*, 2024, **11**, 015007.

51 B. Sun, Z. Wang, Z. Liu, X. Tan, X. Liu, T. Shi, J. Zhou and G. Liao, *Adv. Funct. Mater.*, 2019, **29**, 1900541.

52 L. Chen, C. Yang and C. Yan, *J. Mater. Sci. Technol.*, 2020, **48**, 100–104.

53 H. Zhao, Y. Yan, X. Song, Z. Ma, T. Tian, Y. Jiang, X. Li, C. Xia and J. Li, *Nanoscale*, 2021, **13**, 3757–3766.

54 C. Li, J. Wu, R. Bian, G. Cao, E. Pan, Z. Liu, J. Yu, H. Hosono and F. Liu, *Adv. Funct. Mater.*, 2022, **32**, 2208531.

55 Y. Zhang, F. Wang, X. Zhao, X. Feng, N. Zhang, F. Xia, Y. Ma, H. Li and T. Zhai, *Nanoscale Horiz.*, 2023, **8**, 108–117.

56 Q. Hao, H. Yi, J. Liu, Y. Wang, J. Chen, X. Yin, C. S. Tang, D. Qi, H. Gan, A. T. S. Wee, Y. Chai and W. Zhang, *Adv. Opt. Mater.*, 2022, **10**, 2200063.

57 Q. Ye, J. Lu, Z. Zheng, W. Huang, J. Yao and G. Yang, *Adv. Opt. Mater.*, 2022, **10**, 2102335.

58 L. Xu, M. Yang, Q. Lu, Y. Ren, Y. Chen, J. Guo, M. Cai, X. Miao, F. Teng, H. Fan, C. Zhang, X. He and P. Hu, *Phys. Status Solidi RRL*, 2024, **18**, 2300183.

59 M. Serra, N. Antonatos, J. Luxa, L. Lajaunie, J. Albero, A. Sabik, W. M. Linhart, H. Garcia, R. Kudrawiec, D. Sedmidubský and Z. Sofer, *J. Mater. Chem. C*, 2023, **11**, 6317–6326.

60 Y. Yang, J. Liu, C. Zhao, Q. Liang, W. Dong, J. Shi, P. Wang, D. Kong, L. Lv, L. Jia, D. Wang, S. Zheng, M. Wang, F. Liu, P. Yu, W. Ji, C. Huang, J. Qiao and J. Zhou, *Adv. Mater.*, 2024, **36**, 2307237.

61 L. Zhang, Y. He, X. Dong, J. Guo, Z. Gao, Z. Liu, J. Chen, Y. Zhao, Z. Zhou, J. Yin, X. Fu, F. Luo, H. Fu and J. Wu, *Laser Photonics Rev.*, 2024, **18**, 2300854.

62 X. Meng, Y. Du, W. Wu, N. B. Joseph, X. Deng, J. Wang, J. Ma, Z. Shi, B. Liu, Y. Ma, F. Yue, N. Zhong, P. H. Xiang, C. Zhang, C. G. Duan, A. Narayan, Z. Sun, J. Chu and X. Yuan, *Adv. Sci.*, 2023, **10**, 2300413.

63 T. Guo, Z. Sa, P. Wei, Y. Jian, X. Chen, Z. Chen, J. Avila, P. Dudin, Z. Yang, X. Song, F. Liu and S. Zhang, *2D Mater.*, 2023, **10**, 025004.

64 N. Q. Diep, Y. X. Chen, D. L. Nguyen, M. N. Duong, S. K. Wu, C. W. Liu, H. C. Wen, W. C. Chou, J. Y. Juang, Y. J. Hsu, V. Q. Le, Y. H. Chu and S. H. Huynh, *J. Mater. Chem. C*, 2023, **11**, 1772–1781.

65 Q. Li, S. Wang, J. Xue, Z. Zhou, Y. Hu, Z. Zhou, Z. Feng, Q. Yan, Y. Yu, Y. Weng, R. Tang, X. Su, F. Zheng, L. Fang and L. You, *Phys. Rev. Appl.*, 2023, **19**, 054055.

66 Q. Ye, Z. Deng, H. Yi, W. Wang, J. Lu, Y. Ma, W. Huang, Z. Zheng, C. Ma, C. Du, Y. Zou, J. Yao and G. Yang, *Adv. Opt. Mater.*, 2023, **11**, 2300463.

67 X. Han, G. Xu, J. Xing, Y. Song, Z. Sun, D. Rong, F. Ma, Z. Guo, B. Feng, J.-G. Guo, X. Xu, Y. Wang, Y. Dai and Y. Huang, *Adv. Opt. Mater.*, 2023, **11**, 2300317.

68 C. Y. Zhu, Z. Zhang, J. K. Qin, Z. Wang, C. Wang, P. Miao, Y. Liu, P. Y. Huang, Y. Zhang, K. Xu, L. Zhen, Y. Chai and C. Y. Xu, *Nat. Commun.*, 2023, **14**, 2521.

69 S. Zhang, L. Han, K. Xiao, L. Zhang, C. Shi, L. Xu, K. Deng, Y. Zou, M. Jiang, X. Lv, Y. Zhu, Q. Li, C. Liu, W. Tang, G. Li, S. Ding, X. Chen and W. Lu, *Adv. Funct. Mater.*, 2023, **33**, 2305380.

70 L. Sun, S. Wang, C. Ma, L. Wei, X. Tao and S. Wang, *ACS Appl. Opt. Mater.*, 2024, **2**, 679–686.

71 Z. Zheng, J. Yao, W. Li, L. Huang, Y. Xiao, Z. Mu, G. Yang and J. Li, *J. Mater. Chem. C*, 2018, **6**, 12928–12939.

72 Z. Zheng, P. Chen, J. Lu, J. Yao, Y. Zhao, M. Zhang, M. Hao and J. Li, *Sci. China Mater.*, 2020, **63**, 1560–1569.

73 H. Chen, C. Xie, X. Zhong, Y. Liang, W. Yang, C. Wu and L. Luo, *J. Mater. Chem. C*, 2022, **10**, 6025–6035.

74 H. Gan, Q. Hao, J. Liu, P. Li, D. Qi, F. Liu, T. Lei and W. Zhang, *Adv. Opt. Mater.*, 2022, **10**, 2200033.

75 S. Song, J. Qiao, M. Shen, G. Zhang, F. Feng and M. G. Somekh, *J. Mater. Chem. C*, 2022, **10**, 18174–18181.

76 H. Y. Lee, G. Z. Lu, J. L. Shen, H. Y. Lin and Y. F. Chen, *J. Mater. Chem. C*, 2022, **10**, 16370–16378.

77 S. Akhavan, A. Ruocco, G. Soavi, A. Taheri Najafabadi, S. Mignuzzi, S. Doukas, A. R. Cadore, Y. A. K. Samad, L. Lombardi, K. Dimos, I. Paradisanos, J. E. Muench, H. F. Y. Watson, S. Hodge, L. G. Occhipinti, E. Lidorikis, I. Goykhman and A. C. Ferrari, *2D Mater.*, 2023, **10**, 035015.

78 T. Wang, F. Sun, W. Hong, C. Jian, Q. Ju, X. He, Q. Cai and W. Liu, *J. Mater. Chem. C*, 2023, **11**, 1464–1469.

79 Z. Luo, H. Xu, W. Gao, M. Yang, Y. He, Z. Huang, J. Yao, M. Zhang, H. Dong, Y. Zhao, Z. Zheng and J. Li, *Small*, 2023, **19**, 2207615.

80 B. Moon, J. H. Ahn, M. H. Jeong, S. H. Lee and J. S. Lee, *Adv. Opt. Mater.*, 2023, **11**, 2300414.

81 X. Wang, D. Yan, C. Zhu, Y. Feng, T. Guo, R. Jia, K. Qu, L. Li, T. Zhao, Y. Xiong, A. Farhan, Y. Lin, L. Wu, Y. Dong, S. Zhang, X. Chen and X. Song, *2D Mater.*, 2023, **10**, 045020.

82 S. He, P. Feng, Y. Du, Y. Ma, C. Dang, A. Shan, L. Zhao, T. R. Wei, M. Li and L. Gao, *Adv. Opt. Mater.*, 2024, **12**, 2302399.

83 M. Liu, J. Wei, L. Qi, J. An, X. Liu, Y. Li, Z. Shi, D. Li, K. S. Novoselov, C. W. Qiu and S. Li, *Nat. Commun.*, 2024, **15**, 141.

84 C. Du, H. Gao, Y. Sun, M. Liu, J. Li, J. Sun, J. Leng, W. Wang and K. Li, *J. Alloys Compd.*, 2024, **976**, 173122.

85 R. Ma, Q. Tan, P. Yang, Y. Liu and Q. Wang, *Front. Phys.*, 2024, **19**, 43204.

86 X. L. Zhang, J. Li, B. Leng, L. Yang, Y. D. Song, S. Y. Feng, L. Z. Feng, Z. T. Liu, Z. W. Fu, X. Jiang and B. D. Liu, *Tungsten*, 2023, **5**, 91–99.

87 Z. Jiang, J. Zhou, B. Li, Z. Ma, Z. Huang, Y. Yang, Y. Zhang, Y. Huang, H. Zhang, K. Fan, Y. Li and X. Liu, *Adv. Opt. Mater.*, 2024, **12**, 2302613.

88 N. Zhang, Y. Hao, J. Shao, Y. Chen, J. Yan, Y. Zhang, B. Wang, J. You, L. Gao, Z. Zhong, T. Miao, H. Hu and L. Wang, *IEEE Trans. Electron Devices*, 2023, **70**, 5288–5293.

89 Y. Du, S. Yin, Y. Li, J. Chen, D. Shi, E. Guo, H. Zhang, Z. Wang, Q. Qin, C. Zou, T. Zhai and L. Li, *Small Methods*, 2024, **8**, 2300175.

90 F. He, J. Jiao, Z. Li, L. Yao, R. Ji, D. Wang, Y. Hu, W. Huang, C. Li, G. Lin, F. Wang, F. Zhang and S. Chen, *J. Phys. D: Appl. Phys.*, 2024, **57**, 245107.

91 Z. X. Zhang, T. Haggren, J. X. Li, J. Wang, Q. L. Fang, H. H. Tan and L. B. Luo, *ACS Appl. Nano Mater.*, 2023, **6**, 9917–9927.

92 M. Peng, Z. Wen, M. Shao and X. Sun, *J. Mater. Chem. C*, 2017, **5**, 7521–7526.

93 Z. Zeng, C. Ge, K. Braun, M. Eberle, Y. Wang, B. Zheng, C. Zhu, X. Sun, L. Huang, Z. Luo, Y. Chen, H. Duan, S. Wang, D. Li, F. Gao, A. Pan and X. Wang, *Adv. Funct. Mater.*, 2022, **32**, 2200973.

94 L. Colace, G. Masini, G. Assanto, H. C. Luan, K. Wada and L. C. Kimerling, *Appl. Phys. Lett*, 2000, **76**, 1231–1233.

95 Y. Zhu, V. Raj, Z. Li, H. H. Tan, C. Jagadish and L. Fu, *Adv. Mater.*, 2021, **33**, 2105729.

96 D. Schall, C. Porschatis, M. Otto and D. Neumaier, *J. Phys. D: Appl. Phys*, 2017, **50**, 124004.

97 A. Chatterjee, S. Yadav, S. Kumar Sikdar and S. Kumar Selvaraja, *Opt. Express*, 2020, **28**, 33644–33655.

98 B. Son, Y. Lin, K. H. Lee, J. Margetis, D. Kohen, J. Tolle and C. S. Tan, *IEEE Photonics J.*, 2022, **14**, 1–6.

99 Y. Ye, H. Ma, J. Wu, B. Sun, J. Jian, M. Wei, R. Tang, Y. Shi, H. Lin and L. Li, *IEEE J. Sel. Top. Quantum Electron.*, 2024, **30**, 1–8.

100 N. Flöry, P. Ma, Y. Salamin, A. Emboras, T. Taniguchi, K. Watanabe, J. Leuthold and L. Novotny, *Nat. Nanotechnol.*, 2020, **15**, 118–124.

101 H. Cao, Y. Xiang, W. Sun, J. Xie, J. Guo, Z. Yu, L. Liu, Y. Shi and D. Dai, *ACS Photonics*, 2024, **11**, 1761–1770.

102 L. Li, R. Pan, Z. Xie, Y. Lu, J. Chen, X. Zou, Z. Yuan, M. Chang, H. Lu and B. Chen, *Opt. Express*, 2022, **30**, 20684–20696.

103 Y. Shen, X. Xue, A. H. Jones, Y. Peng, J. Gao, T. C. Tzu, M. Konkol and J. C. Campbell, *Opt. Express*, 2022, **30**, 3047–3054.

104 E. O. Polat, G. Mercier, I. Nikitskiy, E. Puma, T. Galan, S. Gupta, M. Montagut, J. J. Piqueras, M. Bouwens, T. Durduran, G. Konstantatos, S. Goossens and F. Koppens, *Sci. Adv.*, 2019, **5**, eaaw7846.

105 J. Lu, Q. Ye, C. Ma, Z. Zheng, J. Yao and G. Yang, *ACS Nano*, 2022, **16**, 12852–12865.

106 Z. Gao, L. Mei, J. Zhou, Y. Fu, L. Zhai, Z. Li, R. Yang, D. Li, Q. Zhang, J. He, J. Li, X. Huang, H. Li, Y. Liu, K. Yao, Y. Gao, L. Zheng, Y. Chen, D. Lei, H. Zhang, Z. Zeng and X. Yu, *Mater. Today*, 2023, **69**, 31–40.

107 Z. Xing, H. Xiaozong, Y. Jing, L. Shiyuan, S. Zhaowei, Z. Qi, L. Huiqiao, M. Ying, X. Hua and Z. Tianyou, *Adv. Funct. Mater.*, 2023, **33**, 2302474.

108 J. D. Yao, Z. Q. Zheng and G. W. Yang, *Prog. Mater. Sci.*, 2019, **106**, 100573.

109 M. Long, P. Wang, H. Fang and W. Hu, *Adv. Funct. Mater.*, 2019, **29**, 1803807.

110 J. Yao and G. Yang, *J. Appl. Phys*, 2020, **127**, 030902.

111 J. D. Yao and G. W. Yang, *Nano Today*, 2021, **36**, 101026.

112 H. Wang, Z. Li, D. Li, P. Chen, L. Pi, X. Zhou and T. Zhai, *Adv. Funct. Mater.*, 2021, **31**, 2103106.

113 J. Yao and G. Yang, *Adv. Sci.*, 2022, **9**, 2103036.

114 H. Mu, W. Yu, J. Yuan, S. Lin and G. Zhang, *Mater. Futures*, 2022, **1**, 012301.

115 J. Yao and G. Yang, *J. Appl. Phys*, 2022, **131**, 161101.

116 E. Elahi, M. Ahmad, A. Dahshan, M. Rabeel, S. Saleem, V. H. Nguyen, H. H. Hegazy and S. Aftab, *Nanoscale*, 2024, **16**, 14–43.

117 Y. Ma, H. Yi, H. Liang, W. Wang, Z. Zheng, J. Yao and G. Yang, *Mater. Futures*, 2024, **3**, 012301.

118 A. Ahmed, M. Zahir Iqbal, A. Dahshan, S. Aftab, H. H. Hegazy and E. S. Yousef, *Nanoscale*, 2024, **16**, 2097–2120.

119 X. Zhang, R. Li, Y. Yu, F. Dai, R. Jiang, J. Guo, W. Hu, Z. Ni and J. Lu, *Laser Photonics Rev.*, 2024, **18**, 2300936.

120 Y. Li, W. Yu, K. Zhang, N. Cui, T. Yun, X. Xia, Y. Jiang, G. Zhang, H. Mu and S. Lin, *Mater. Horiz.*, 2024, **11**, 2572–2602.

121 Z. Cheng, T. Zhao and H. Zeng, *Small Science*, 2022, **2**, 2100051.

122 J. Zhang, Y. Huang, Z. Tan, T. Li, Y. Zhang, K. Jia, L. Lin, L. Sun, X. Chen, Z. Li, C. Tan, J. Zhang, L. Zheng, Y. Wu, B. Deng, Z. Chen, Z. Liu and H. Peng, *Adv. Mater.*, 2018, **30**, 1803194.

123 F. Sun, H. Xu, W. Hong, Z. Sun and W. Liu, *Adv. Funct. Mater.*, 2024, **34**, 2313776.

124 Z. Zhao, D. Wu, J. Guo, E. Wu, C. Jia, Z. Shi, Y. Tian, X. Li and Y. Tian, *J. Mater. Chem. C*, 2019, **7**, 12121–12126.

125 L. Gao, B. Yang, J. Du, C. Zhang, S. Ma, Z. Guo, Y. Wang, J. Wang, X. Li, D. Wu and P. Lin, *Nanoscale*, 2024, **16**, 12228–12236.

126 J. Zhang, Z. Sa, P. Li, Z. Zhai, F. Liu, M. Wang, G. Wang, Y. Yin, Y. Li, W. Mu, Z. Jia, F. Chen and Z. Yang, *Adv. Opt. Mater.*, 2024, **12**, 2302665.

127 J. Zhang, M. Wang, P. Li, Z. Sa, F. Liu, W. Sun, Y. Li, W. Mu, Z. Jia, M. Chen and Z. Yang, *ACS Appl. Mater. Interfaces*, 2024, **16**, 3685–3693.

128 Q. Zhang, Z. Wu, X. Chen, W. Gao, M. Yang, Y. Xiao, J. Yao, Y. Liang, Z. Zheng, L. Tao and J. Li, *Adv. Opt. Mater.*, 2024, **12**, 2302958.

129 D. Wu, J. Guo, C. Wang, X. Ren, Y. Chen, P. Lin, L. Zeng, Z. Shi, X. J. Li, C. X. Shan and J. Jie, *ACS Nano*, 2021, **15**, 10119–10129.

130 L. Zeng, D. Wu, J. Jie, X. Ren, X. Hu, S. P. Lau, Y. Chai and Y. H. Tsang, *Adv. Mater.*, 2020, **32**, 2004412.

131 N. Guo, W. Hu, T. Jiang, F. Gong, W. Luo, W. Qiu, P. Wang, L. Liu, S. Wu, L. Liao, X. Chen and W. Lu, *Nanoscale*, 2016, **8**, 16065–16072.

132 M. Engel, M. Steiner and P. Avouris, *Nano Lett.*, 2014, **14**, 6414–6417.

133 H. Wang, S. Chen and X. Chen, *Nano Lett.*, 2024, **24**, 326–330.

134 D. Wu, C. Jia, F. Shi, L. Zeng, P. Lin, L. Dong, Z. Shi, Y. Tian, X. Li and J. Jie, *J. Mater. Chem. A*, 2020, **8**, 3632–3642.

135 D. Wu, J. Guo, J. Du, C. Xia, L. Zeng, Y. Tian, Z. Shi, Y. Tian, X. J. Li, Y. H. Tsang and J. Jie, *ACS Nano*, 2019, **13**, 9907–9917.

136 X. Li, K. Liu, R. Zhuo, L. Zeng, P. Lin, L. Li, Z. Shi, Y. Tian, X. Li and D. Wu, *ACS Photonics*, 2024, **11**, 2070–2076.

137 C. Guo, Y. Hu, G. Chen, D. Wei, L. Zhang, Z. Chen, W. Guo, H. Xu, C. N. Kuo and C. S. Lue, *Sci. Adv.*, 2020, **6**, eabb6500.

138 L. Vicarelli, M. S. Vitiello, D. Coquillat, A. Lombardo, A. C. Ferrari, W. Knap, M. Polini, V. Pellegrini and A. Tredicucci, *Nat. Mater.*, 2012, **11**, 865–871.

139 W. Tang, A. Politano, C. Guo, W. Guo, C. Liu, L. Wang, X. Chen and W. Lu, *Adv. Funct. Mater.*, 2018, **28**, 1801786.

140 L. Viti, D. Coquillat, A. Politano, K. A. Kokh, Z. S. Aliev, M. B. Babanly, O. E. Tereshchenko, W. Knap, E. V. Chulkov and M. S. Vitiello, *Nano Lett.*, 2016, **16**, 80–87.

141 H. Xu, C. Guo, J. Zhang, W. Guo, C. N. Kuo, C. S. Lue, W. Hu, L. Wang, G. Chen, A. Politano, X. Chen and W. Lu, *Small*, 2019, **15**, 1903362.

142 S. Guo, Y. He, X. Lv, M. Jiang, Y. Wei, Y. Deng, X. Pan, S. Lan, D. Wang, A. Liu, C. Guo and L. Wang, *2D Mater.*, 2024, **11**, 035008.

143 L. Yang, D. Wang, Z. Dong, Y. Zhang, L. Huang, J. Zhang, P. Wang, C. Chen, J. Li, J. Wang, L. Wang and K. Zhang, *IEEE Electron Device Lett.*, 2023, **44**, 686–689.

144 Z. Hu, L. Zhang, A. Chakraborty, G. D'Olimpio, J. Fujii, A. Ge, Y. Zhou, C. Liu, A. Agarwal, I. Vobornik, D. Farias, C. N. Kuo, C. S. Lue, A. Politano, S. W. Wang, W. Hu, X. Chen, W. Lu and L. Wang, *Adv. Mater.*, 2023, **35**, 2209557.

145 L. Zhang, Z. Dong, L. Wang, Y. Hu, C. Guo, L. Guo, Y. Chen, L. Han, K. Zhang, S. Tian, C. Yao, Z. Chen, M. Cai, M. Jiang, H. Xing, X. Yu, X. Chen, K. Zhang and W. Lu, *Adv. Sci.*, 2021, **8**, 2102088.

146 C. Guo, Z. Chen, X. Yu, L. Zhang, X. Wang, X. Chen and L. Wang, *Nano Lett.*, 2022, **22**, 7492–7498.

147 J. Shen, H. Xing, L. Wang, Z. Hu, L. Zhang, X. Wang, Z. Chen, C. Yao, M. Jiang, F. Fei, G. Chen, L. Han, F. Song and X. Chen, *Appl. Phys. Lett*, 2022, **120**, 063501.

148 Y. He, L. Yang, Z. Hu, L. Zhang, X. Pan, Y. Wei, S. Guo, X. Lv, M. Jiang, L. Han, D. Wang, S. Lan, X. Sun, X. Chen, K. Zhang and L. Wang, *Adv. Funct. Mater.*, 2024, **34**, 2311008.

149 D. Wu, C. Guo, L. Zeng, X. Ren, Z. Shi, L. Wen, Q. Chen, M. Zhang, X. J. Li, C. X. Shan and J. Jie, *Light: Sci. Appl.*, 2023, **12**, 5.

150 P. Ye, H. Xiao, Q. Zhu, Y. Kong, Y. Tang and M. Xu, *Sci. China Mater.*, 2023, **66**, 193–201.

151 H. Zhang, M. Holbrook, F. Cheng, H. Nam, M. Liu, C. R. Pan, D. West, S. Zhang, M. Y. Chou and C. K. Shih, *ACS Nano*, 2021, **15**, 2497–2505.

152 M. S. Claro, J. Grzonka, N. Nicoara, P. J. Ferreira and S. Sadewasser, *Adv. Opt. Mater.*, 2021, **9**, 2001034.

153 Q. Ye, D. Xu, B. Cai, J. Lu, H. Yi, C. Ma, Z. Zheng, J. Yao, G. Ouyang and G. Yang, *Mater. Horiz.*, 2022, **9**, 2364–2375.

154 J. Yao, Z. Zheng and G. Yang, *ACS Appl. Mater. Interfaces*, 2016, **8**, 12915–12924.

155 S. Song, S. Jeon, M. Rahaman, J. Lynch, D. Rhee, P. Kumar, S. Chakravarthi, G. Kim, X. Du and E. W. Blanton, *Matter*, 2023, **6**, 3483–3498.

156 X. Tang, S. Wang, Y. Liang, D. Bai, J. Xu, Y. Wang, C. Chen, X. Liu, S. Wu, Y. Wen, D. Jiang and Z. Zhang, *Phys. Chem. Chem. Phys.*, 2022, **24**, 7323–7330.

157 Y. Zou, Z. Zhang, J. Yan, L. Lin, G. Huang, Y. Tan, Z. You and P. Li, *Nat. Commun.*, 2022, **13**, 4372.

158 M. F. Khan, S. Sadaqat, M. A. Khan, S. Rehman, W. S. Subhani, M. Ouladsmane, M. A. Rehman, F. Ali, H. Lipsanen, Z. Sun, J. Eom and F. Ahmed, *Nanoscale*, 2024, **16**, 3622–3630.

159 W. Feng, F. Gao, Y. Hu, M. Dai, H. Li, L. Wang and P. Hu, *Nanotechnology*, 2018, **29**, 445205.

160 Z. Q. Zheng, J. D. Yao and G. W. Yang, *J. Mater. Chem. C*, 2016, **4**, 8094–8103.

161 Z. Zheng, J. Yao and G. Yang, *ACS Appl. Mater. Interfaces*, 2017, **9**, 14920–14928.

162 Y. Gong, B. Li, G. Ye, S. Yang, X. Zou, S. Lei, Z. Jin, E. Bianco, S. Vinod, B. I. Yakobson, J. Lou, R. Vajtai, W. Zhou and P. M. Ajayan, *2D Mater.*, 2017, **4**, 021028.

163 S. R. Weng, W. L. Zhen, X. Yan, Z. L. Yue, H. J. Hu, F. Xu, R. R. Zhang, L. Pi, W. K. Zhu and C. J. Zhang, *J. Phys.: Condens. Matter*, 2021, **33**, 395001.

164 R. Zhang, Z. Yang, L. Liu, J. Lin, S. Wen, Y. Meng, Y. Yin, C. Lan, C. Li, Y. Liu and J. C. Ho, *Adv. Opt. Mater.*, 2023, **11**, 2301055.

165 H. Yuan, X. Liu, F. Afshinmanesh, W. Li, G. Xu, J. Sun, B. Lian, A. G. Curto, G. Ye, Y. Hikita, Z. Shen, S. C. Zhang, X. Chen, M. Brongersma, H. Y. Hwang and Y. Cui, *Nat. Nanotechnol.*, 2015, **10**, 707–713.

166 H. Liu, C. Zhu, Y. Chen, X. Yi, X. Sun, Y. Liu, H. Wang, G. Wu, J. Wu, Y. Li, X. Zhu, D. Li and A. Pan, *Adv. Funct. Mater.*, 2024, **34**, 2314838.

167 F. Wang, S. Zhu, W. Chen, J. Han, R. Duan, C. Wang, M. Dai, F. Sun, Y. Jin and Q. J. Wang, *Nat. Nanotechnol.*, 2024, **19**, 455–462.

168 X. Xie, J. Ding, B. Wu, H. Zheng, S. Li, C. T. Wang, J. He, Z. Liu, J. T. Wang, J. Duan and Y. Liu, *Nanoscale*, 2023, **15**, 12388–12397.

169 J. Wang, N. Han, Z. Lin, S. Hu, R. Tian, M. Zhang, Y. Zhang, J. Zhao and X. Gan, *Nanoscale*, 2024, **16**, 3101–3106.

170 Y. Pan, T. Zheng, F. Gao, L. Qi, W. Gao, J. Zhang, L. Li, K. An, H. Gu and H. Chen, *Small*, 2024, 2311606.

171 S. Zhu, R. Duan, X. Xu, F. Sun, W. Chen, F. Wang, S. Li, M. Ye, X. Zhou, J. Cheng, Y. Wu, H. Liang, J. Kono, X. Li, Z. Liu and Q. J. Wang, *Light: Sci. Appl.*, 2024, **13**, 119.

172 L. Kong, G. Li, Q. Su, X. Tan, X. Zhang, Z. Liu, G. Liao, B. Sun and T. Shi, *ACS Appl. Mater. Interfaces*, 2023, **15**, 43135–43144.

173 F. Yan, L. Zhao, A. Patanè, P. Hu, X. Wei, W. Luo, D. Zhang, Q. Lv, Q. Feng and C. Shen, *Nanotechnology*, 2017, **28**, 27LT01.

174 Q. Lv, F. Yan, X. Wei and K. Wang, *Adv. Opt. Mater.*, 2018, **6**, 1700490.

175 Z. Zheng, J. Yao, B. Wang and G. Yang, *Nanotechnology*, 2017, **28**, 415501.

176 J. Yao and G. Yang, *Small*, 2018, **14**, 1704524.

177 A. Abnavi, R. Ahmadi, H. Ghanbari, M. Fawzy, A. Hasani, T. De Silva, A. M. Askar, M. R. Mohammadzadeh, F. Kabir, M. Whitwick, M. Beaudoin, S. K. O'Leary and M. M. Adachi, *Adv. Funct. Mater.*, 2023, **33**, 2210619.

178 X. Zhang, D. Qiu, P. Zhou and P. Hou, *Appl. Phys. Lett*, 2024, **124**, 042108.

179 Y. Lu, T. Chen, N. Mkhize, R. J. Chang, Y. Sheng, P. Holdway, H. Bhaskaran and J. H. Warner, *ACS Nano*, 2021, **15**, 19570–19580.

180 X. Zhou, Q. Zhang, L. Gan, H. Li and T. Zhai, *Adv. Funct. Mater.*, 2016, **26**, 4405–4413.

181 J. Yao, Z. Zheng and G. Yang, *Adv. Funct. Mater.*, 2017, **27**, 1701823.

182 Q. Ji, C. Li, J. Wang, J. Niu, Y. Gong, Z. Zhang, Q. Fang, Y. Zhang, J. Shi and L. Liao, *Nano Lett.*, 2017, **17**, 4908–4916.

183 H. Bark, Y. Choi, J. Jung, J. H. Kim, H. Kwon, J. Lee, Z. Lee, J. H. Cho and C. Lee, *Nanoscale*, 2018, **10**, 1056–1062.

184 B. Wei, Y. Li, T. Yun, Y. Li, T. Gui, W. Yu, H. Mu, N. Cui, W. Chen and S. Lin, *Mater. Futures*, 2024, **3**, 025302.

185 S. Gao, J. Xu, S. Shi, J. Chen, J. Xu, L. Kong, X. Zhang and L. Li, *Adv. Opt. Mater.*, 2024, **12**, 2302141.

186 J. W. Kang, C. Zhang, K. J. Cao, Y. Lu, C. Y. Wu, S. R. Chen, D. Wu, C. Xie and L. B. Luo, *J. Mater. Chem. C*, 2020, **8**, 13762–13769.

187 M. Ma, H. Chen, K. Zhou, C. Xie, Y. Liang, L. Wang, C. Wu, W. Yang, J. Guo and L. Luo, *J. Mater. Chem. C*, 2021, **9**, 2823–2832.

188 Q. Yang, Z. D. Luo, D. Zhang, M. Zhang, X. Gan, J. Seidel, Y. Liu, Y. Hao and G. Han, *Adv. Funct. Mater.*, 2022, **32**, 2207290.

189 Z. Zhang, C. Sun, B. Zhu, J. Chen, Z. Fu, Z. Li, S. Wu, Y. Zhang, J. Cai, R. Hong, D. Lin, D. Fu, Z. Wu, X. Chen and F. Zhang, *Adv. Opt. Mater.*, 2024, 2400469.

190 H. J. Lee, W. G. Hong, H. Y. Yang, D. H. Ha, Y. Jun and Y. J. Yun, *Adv. Mater. Technol.*, 2022, **7**, 2100709.

191 K. Y. Lian, Y. F. Ji, X. F. Li, M. X. Jin, D. J. Ding and Y. Luo, *J. Phys. Chem. C*, 2013, **117**, 6049–6054.

192 A. Mathkar, D. Tozier, P. Cox, P. Ong, C. Galande, K. Balakrishnan, A. Leela Mohana Reddy and P. M. Ajayan, *J. Phys. Chem. Lett.*, 2012, **3**, 986–991.

193 A. J. Cho and J. Y. Kwon, *ACS Appl. Mater. Interfaces*, 2019, **11**, 39765–39771.

194 F. Wu, Q. Li, P. Wang, H. Xia, Z. Wang, Y. Wang, M. Luo, L. Chen, F. Chen, J. Miao, X. Chen, W. Lu, C. Shan, A. Pan, X. Wu, W. Ren, D. Jariwala and W. Hu, *Nat. Commun.*, 2019, **10**, 4663.

195 K. Nassiri Nazif, A. Daus, J. Hong, N. Lee, S. Vaziri, A. Kumar, F. Nitta, M. E. Chen, S. Kananian, R. Islam, K. H. Kim, J. H. Park, A. S. Y. Poon, M. L. Brongersma, E. Pop and K. C. Saraswat, *Nat. Commun.*, 2021, **12**, 7034.

196 C. Junwei, W. Fengmei, Y. Lei, L. Le, Y. Chaoyi, W. Feng, W. Yao, W. Zhenxing, J. Chao, F. Liping, X. Jie, L. Yanrong and H. Jun, *Adv. Funct. Mater.*, 2017, **27**, 1701342.

197 Y. Yan, W. Xiong, S. Li, K. Zhao, X. Wang, J. Su, X. Song, X. Li, S. Zhang, H. Yang, X. Liu, L. Jiang, T. Zhai, C. Xia, J. Li and Z. Wei, *Adv. Opt. Mater.*, 2019, **7**, 1900622.

198 M. Zhong, K. Zhou, Z. Wei, Y. Li, T. Li, H. Dong, L. Jiang, J. Li and W. Hu, *2D Mater.*, 2018, **5**, 035033.

199 H. Long, H. Liu, H. Wang, B. Wang, R. Bai, Y. Yu, K. Xin, L. Liu, Y. Xu, J. Zhang, F. Jiang, X. Wang, Z. Wei and J. Yang, *Adv. Funct. Mater.*, 2023, **33**, 2306241.

200 Y. Yan, J. Yang, J. Du, X. Zhang, Y. Y. Liu, C. Xia and Z. Wei, *Adv. Mater.*, 2021, **33**, 2008761.

201 H. Liu, J. Meng, X. Zhang, Y. Chen, Z. Yin, D. Wang, Y. Wang, J. You, M. Gao and P. Jin, *Nanoscale*, 2018, **10**, 5559–5565.

202 F. Cao, Z. Li, X. Liu, Z. Shi and X. Fang, *Adv. Funct. Mater.*, 2022, **32**, 2206151.

203 X. Zhang, Z. Li, E. Hong, M. Deng, L. Su and X. Fang, *Adv. Funct. Mater.*, 2024, 2312293.

204 J. Lei, T. Zheng, W. Wu, Z. Zheng, Q. Zheng, X. Wang, W. Xiao, J. Li and M. Yang, *Sci. China Mater.*, 2024, **67**, 863–870.

205 C. Zhang, S. Peng, J. Han, C. Li, H. Zhou, H. Yu, J. Gou, C. Chen, Y. Jiang and J. Wang, *Adv. Funct. Mater.*, 2023, **33**, 2302466.

206 L. Zeng, W. Han, X. Ren, X. Li, D. Wu, S. Liu, H. Wang, S. P. Lau, Y. H. Tsang, C. X. Shan and J. Jie, *Nano Lett.*, 2023, **23**, 8241–8248.

207 T. L. Singal, *Optical fiber communications: principles and applications*, Cambridge University Press, 2016.

208 W. R. Syong, J. H. Fu, Y. H. Kuo, Y. C. Chu, M. Hakami, T. Y. Peng, J. Lynch, D. Jariwala, V. Tung and Y. J. Lu, *ACS Nano*, 2024, **18**, 5446–5456.

209 J. Xiong, Q. Yu, X. Hou, B. Liu, S. Li, H. Deng, Z. Yang, J. Leng, S. Zhu, Y. Sun, Z. Jiang, N. Huo, J. Wu and P. Zhou, *Adv. Funct. Mater.*, 2024, **34**, 2314972.

210 K. Du, M. Wang, Z. Liang, Q. Lv, H. Hou, S. Lei, G. Liu, J. Liu and G. Qiao, *Appl. Phys. Lett*, 2024, **124**, 063508.

211 S. Li, Y. Yan, J. Li, M. Qian, C. Shen, X. Song, Y. Jiang, C. Xia and J. Li, *Appl. Phys. Lett*, 2022, **121**, 112101.

212 W. Ma, T. Wu, N. Yao, W. Zhou, L. Jiang, Q. Qiu, J. Li and Z. Huang, *Commun. Mater.*, 2022, **3**, 68.

213 F. Wang, L. Li, W. Huang, L. Li, B. Jin, H. Li and T. Zhai, *Adv. Funct. Mater.*, 2018, **28**, 1802707.

214 J. Yao, J. Shao, Y. Wang, Z. Zhao and G. Yang, *Nanoscale*, 2015, **7**, 12535–12541.

215 J. Yao, Z. Zheng and G. Yang, *J. Mater. Chem. C*, 2016, **4**, 7831–7840.

216 H. Liu, X. Zhu, X. Sun, C. Zhu, W. Huang, X. Zhang, B. Zheng, Z. Zou, Z. Luo, X. Wang, D. Li and A. Pan, *ACS Nano*, 2019, **13**, 13573–13580.

217 M. Yu, C. Fang, J. Han, W. Liu, S. Gao and K. Huang, *ACS Appl. Mater. Interfaces*, 2022, **14**, 13507–13515.

218 Y. Lu, X. Sun, H. Zhou, H. Lai, R. Liu, P. Liu, Y. Zhou and W. Xie, *Appl. Phys. Lett*, 2022, **121**, 161104.

219 T. Zheng, M. Yang, Y. Pan, Z. Zheng, Y. Sun, L. Li, N. Huo, D. Luo, W. Gao and J. Li, *ACS Appl. Mater. Interfaces*, 2023, **15**, 29363–29374.

220 M. Yu, F. Zhang, W. Gao, H. Shen, L. Kang, L. Ju and H. Yin, *Phys. Chem. Chem. Phys.*, 2023, **25**, 29241–29248.

221 S. Chen, B. Cao, W. Wang, X. Tang, Y. Zheng, J. Chai, D. Kong, L. Chen, S. Zhang and G. Li, *Appl. Phys. Lett.*, 2022, **120**, 111101.

222 H. Yi, C. Ma, W. Wang, H. Liang, R. Cui, W. Cao, H. Yang, Y. Ma, W. Huang, Z. Zheng, Y. Zou, Z. Deng, J. Yao and G. Yang, *Mater. Horiz.*, 2023, **10**, 3369–3381.

223 Y. Ma, C. Ma, H. Yi, H. Liang, W. Wang, Z. Zheng, Y. Zou, Z. Deng, J. Yao and G. Yang, *Adv. Opt. Mater.*, 2024, **12**, 2302039.

224 A. Cao, S. Li, H. Chen, M. Deng, X. Xu, L. Shang, Y. Li, A. Cui and Z. Hu, *Mater. Horiz.*, 2023, **10**, 5099–5109.

225 S. Zhang, A. Hu, Q. Liu, L. Xu, X. Ren, B. Wang, Y. Ren, W. Liu, X. Zhou, S. Chen and X. Guo, *Adv. Electron. Mater.*, 2023, **9**, 2300243.

226 M. Massicotte, P. Schmidt, F. Vialla, K. G. Schädler, A. Reserbat-Plantey, K. Watanabe, T. Taniguchi, K. J. Tielrooij and F. H. L. Koppens, *Nat. Nanotechnol.*, 2016, **11**, 42–46.

227 M. Dai, H. Chen, F. Wang, M. Long, H. Shang, Y. Hu, W. Li, C. Ge, J. Zhang, T. Zhai, Y. Fu and P. Hu, *ACS Nano*, 2020, **14**, 9098–9106.

228 Z. Luo, M. Yang, D. Wu, Z. Huang, W. Gao, M. Zhang, Y. Zhou, Y. Zhao, Z. Zheng and J. Li, *Small Methods*, 2022, **6**, 2200583.

229 Y. Niu, X. Zhou, W. Gao, M. Fu, Y. Duan, J. Yao, B. Wang, M. Yang, Z. Zheng and J. Li, *ACS Nano*, 2023, **17**, 13760–13768.

230 M. Wichmann, M. Kamil, A. Frederiksen, S. Kotzur and M. Scherl, *IEEE Sens. J.*, 2022, **22**, 2024–2036.

231 S. Kurtti, A. Baharmast, J. P. Jansson and J. Kostamovaara, *IEEE Sens. J.*, 2021, **21**, 22944–22955.

232 J. Fu, C. Nie, F. Sun, G. Li, H. Shi and X. Wei, *Sci. Adv.*, 2024, **10**, eadk8199.

233 M. Zhang, G. Zeng, G. Wu, J. Zeng, Y. Sun, C. Li, L. Liu, J. Wang, H. L. Lu, Y. Chai and J. Wang, *Appl. Phys. Lett.*, 2023, **122**, 253503.

234 J. Lu, Z. Deng, Q. Ye, Z. Zheng, J. Yao and G. Yang, *Small Methods*, 2022, **6**, 2101046.

235 T. H. Tsai, Z. Y. Liang, Y. C. Lin, C. C. Wang, K. I. Lin, K. Suenaga and P. W. Chiu, *ACS Nano*, 2020, **14**, 4559–4566.

236 H. Jiang, J. Fu, J. Wei, S. Li, C. Nie, F. Sun, Q. Y. S. Wu, M. Liu, Z. Dong, X. Wei, W. Gao and C. W. Qiu, *Nat. Commun.*, 2024, **15**, 1225.

237 S. Kim, W. Lee, K. Ko, H. Cho, H. Cho, S. Jeon, C. Jeong, S. Kim, F. Ding and J. Suh, *Adv. Mater.*, 2024, 2400800.

238 S. Liu, X. Yuan, P. Wang, Z. G. Chen, L. Tang, E. Zhang, C. Zhang, Y. Liu, W. Wang, C. Liu, C. Chen, J. Zou, W. Hu and F. Xiu, *ACS Nano*, 2015, **9**, 8592–8598.

239 Y. Xia, X. Chen, J. Wei, S. Wang, S. Chen, S. Wu, M. Ji, Z. Sun, Z. Xu, W. Bao and P. Zhou, *Nat. Mater.*, 2023, **22**, 1324–1331.